

Geometric Characteristics of Coarse-sand Ripples Generated by Oscillatory Flows: A Full-Scale Experimental Study

Dongxu Wang^a, Jing Yuan^a

^a*Department of Civil and Environmental Engineering, National University of Singapore,
1 Engineering Dr. 2, Block E1A 07-03, Singapore 117576*

Abstract

The shape of vortex ripples generated by wave boundary layers determines the local hydrodynamics and sediment motions, and therefore is critical for understanding coastal sediment transport in the rippled-bed regime. In this study, coarse-sand vortex ripples were generated by periodic oscillatory flows mimicking full-scale field conditions in an oscillatory water tunnel. A laser-based bottom profiler was applied for measuring the movable bed's profile. The observed ripple development from a flat bed is in agreement with many previous studies. Small ripple marks appeared within a couple of flow periods, and gradually became 3-dimensional (3-D) transient ripples, which eventually evolved to equilibrium 2-dimensional (2-D) ripples after $O(100-1000)$ flow periods. The shape of equilibrium 2-D ripple was studied based on a representative ripple profile obtained by ensemble averaging a periodic ripple train. The shape of ripples formed under sinusoidal flows become increasingly sinusoidal as the flow becomes stronger (larger Shields parameter) or wave period becomes longer, which is possibly because the influence of coherent vortex becomes more significant. Wave nonlinearities have differ-

ent effects on the ripple shape. Generally speaking, wave skewness makes ripples onshore-leaning while wave asymmetry makes ripples' crests sharper and troughs flatter. Our measurements also revealed some detailed geometric characteristics, i.e., the roundness of ripple crests and the maximum local slope along ripple flanks.

Keywords: vortex ripples, ripple profile, ripple development, skewed and asymmetric flows, oscillatory water tunnel

1. Introduction

In coastal regions, wave-generated sand ripples are usually small-scale bedforms with typical ripple height of $O(10 \sim 100)$ mm and ripple length of $O(100 \sim 1000)$ mm. For ripples with large steepness, a coherent vortex is produced when the wave-driven boundary layer flow separates after passing the ripple crest. The vortex is subsequently shed from the ripple surface to higher levels when the sediment-laden oscillatory flow reverses, leading to a considerable suspended-load sediment transport rate. Therefore, these ripples are usually referred to as vortex ripples. The formation of the coherent vortex is controlled by ripple shape, so a direct modeling of sediment transport over vortex ripples requires a good understanding of ripple geometry under various sediment-flow conditions.

The majority of previous studies regarding the ripple geometry focused on the dimension of equilibrium ripples, which is usually quantified by two key parameters: ripple length λ and height η . Bagnold and Taylor (1946) in their pioneering study measured the length of vortex ripples and claimed that λ is correlated with both sediment grain size and the near-bed water excursion

amplitude A_{bm} . Since then, many researchers aimed at measuring the equilibrium ripple dimension through laboratory experiments (e.g., Lofquist, 1978; Du Toit and Sleath, 1981; Ribberink and Al-Salem, 1994; Faraci and Foti, 2002; Davies and Thorne, 2005; Doucette and O’donoghue, 2006; Pedocchi and García, 2009b) or fields surveys (e.g., Inman, 1957; Dingler, 1974; Miller and Komar, 1980; Nielsen, 1984; Traykovski et al., 1999; Xu, 2005), as summarized in Table 1. Using the established dataset, a few empirical predictive formulas have been developed, which relate ripple dimensions to sediment-flow conditions (e.g., Nielsen, 1981; Grant and Madsen, 1982; Wiberg and Harris, 1994; Faraci and Foti, 2002; Pedocchi and García, 2009a). There are, however, very little detailed measurements on ripple shape, i.e., most studies cited in Table 1 only provided qualitative descriptions on ripple shape (e.g., saying that ripples are round-crested).

Shoaling waves contain both skewness and asymmetry due to the influence of changing water depth. Skewed waves have sharp crests but long and flat troughs, while asymmetric waves have a sawtooth shape with a relatively steeper wave front. These nonlinear features in wave shapes also appear in the near-bed orbital flow motion and therefore alter the ripple shape. In some field studies (e.g., Dingler, 1974), it has been observed that ripples have onshore-leaning shapes. Note that ripples under sinusoidal or “linear” oscillatory flows should be symmetric regarding their crests, so this onshore-leaning feature is possibly due to the nonlinearity of field waves. Recently, van der Werf et al. (2007) studied rippled-bed sediment transport under purely skewed oscillatory flows using an oscillatory water tunnel. Their measurements of ripple shape clearly showed that flow skewness will make the

ripple onshore-leaning. The effect of flow asymmetry, however, is not well documented in the literature, to the authors' knowledge.

The ripple-shape effects on fluid mechanics and sediment transport have already raised researchers' attentions. The presence of ripples leads to a significant increase of flow resistance. In some existing empirical formula, the total bottom roughness for ripple bed k_m , is solely scaled with ripple height, e.g., $k_m = 4\eta$ proposed by Wikramanayake and Madsen (1994). Some researchers (e.g., Nielsen, 1981; Ribberink, 1998) argued that k_m increases with the ripple steepness η/λ , which was confirmed by some experimental studies, e.g., the recent work by Yuan and Wang (2018). Barr et al. (2004) conducted a large-eddy simulation of oscillatory flows over fixed vortex ripples. Three ripple profiles with identical η/λ but different ripple shapes were adopted in the simulations. The calculated total flow resistance was indeed heavily controlled by the ripple shape. From the aspect of sediment transport, it is understandable that the coherent vortex motion and the associated sediment suspension are affected by the ripple shape. The simple "grab-and-dump" concept (e.g., Nielsen, 1988; Shimamoto et al., 2013) had been proposed to describe the effect of coherent vortex, i.e., vortex grabs sediment into suspension during their formation stage, and dumps the sediment back to the ripple surface after being ejected to higher levels. Ripple shape is relevant to the "grab-and-dump" concept, because steeper ripple flanks can trigger stronger flow separation, and therefore entrain more sediment into suspension. Recently, Wang and Yuan (2018) conducted an experimental study on bottom-slope-induced net sediment transport over vortex ripples. They found that ripples become upslope-leaning on sloping bottoms, which can

increase the downslope net transport rate, if the upslope leaning becomes very significant.

Vortex ripples can have different planform geometry, i.e., either two-dimensional (2-D) or three-dimensional (3-D). 2-D ripples have straight and parallel crest lines that are perpendicular to the principle flow direction, and the ripple train is usually quite periodic. 3-D ripples, however, have irregular shapes and very little periodicity. A number of criteria can be found in the literature for the prediction of the planform geometry of ripples (e.g., Carstens et al., 1969; Lofquist, 1978; Pedocchi and Garca, 2009a). Most of them suggest more three-dimensionality for finer sand, longer excursion amplitudes A_{bm} and higher oscillation velocities U_{bm} . This is because flows with larger A_{bm} and (or) U_{bm} can induce more significant lee-side vortex, which contains chaotic 3-D turbulent structures. Finer sand grains have less inertia to withstand these 3-D effects and thus usually form 3-D ripples.

Studying 2-D ripples is usually the start point for understanding sediment transport over vortex ripples. A few conceptual 2-D ripple shapes had been proposed in the open literature. By only considering pure bedload sediment transport and requiring zero net sediment transport rates everywhere under oscillatory flows with symmetric half periods, Fredsoe and Deigaard (1992) theoretically derived a ripple shape consisting of two parabolas. This profile is highly conceptual since there is an unrealistic sharp crest as the joint of two parabolas. Du Toit and Sleath (1981) generalized another ripple profile based on their laboratory experiments with sinusoidal oscillatory flows, which has parabolic-alike flanks but a smooth transition at the crest. Overall speaking, the crest is sharper and narrower than the trough, which agrees

with most laboratory observations. This profile was adopted in many numerical simulations of boundary layer flows over vortex ripples (e.g., Blondeaux and Vittori, 1991; Davies and Villaret, 1994; Blondeaux et al., 2004). Sinusoidal profile, as a simple shape with symmetric crest and trough, was also adopted in modeling works, e.g., the large eddy simulation (LES) by Chang and Scotti (2003).

One important issue to be highlighted here is the scale effect in most laboratory observations. The scale of near-bed oscillatory flow is characterized by a wave Reynolds number $Re_w = U_{bm}A_{bm}/\nu$, where ν is the water kinematic viscosity. Re_w for forming typical vortex ripples under field conditions can usually reach $O(10^5)$. In small-scale wave flumes or oscillating tray rigs, Re_w is only of $O(10^3 - 10^4)$ due to the facility limits (see Table 1). For example, the ripple profile proposed by Du Toit and Sleath (1981) was based on the measurements with $Re_w = 6.3 \times 10^3 - 5.6 \times 10^4$. Whether this ripple profile can be applied for full-scale conditions is not verified yet. Oscillatory water tunnels (OWT) can easily mimic the full-scale wave boundary layer flows and were widely used in studying vortex ripple dimensions (e.g., O’Donoghue et al., 2006; Pedocchi and Garca, 2009a) and sediment suspensions over vortex ripples (e.g., O’Donoghue and Wright, 2004; van der Werf et al., 2007). More research effort is needed to understand whether the aforementioned ripple profiles can describe full-scale 2-D vortex ripples. In addition, it is also necessary to explore how wave nonlinearity (i.e., skewness and asymmetry) affects the ripple shape through controllable laboratory experiments, since such measurements were very insufficient.

The main objective of this study is to report high-quality measurements

regarding ripple development and detailed shape of 2-D equilibrium ripples under full-scale oscillatory flows. Using a novel OWT, a number of tests covering Re_w from 5.77×10^4 to 1.39×10^6 were reported. These tests were divided into two groups, one for sinusoidal-flow tests and the other for skewed- and asymmetric-flow tests. In most cases, 2-D equilibrium ripples were developed from a coarse-sand movable bed and the bottom profiles were measured using a laser-based bottom profiler (LBP). The paper outline is as follows. Section 2 introduces the experimental setup and test conditions. Section 3-4 show the tests with sinusoidal flows, including ripple development and equilibrium ripple shapes. Section 5 presents the effects of flow nonlinearity on ripple shape. Discussions and conclusions are provided in section 6.

2. Experimental setup and test conditions

2.1. Experimental facility and instruments

Full-scale experiments were conducted in the Wave-Current-Sediment (WCS) facility, which is essentially an OWT, at the Hydraulic Engineering Lab of National University of Singapore. As shown in Figure 1a, the main part of WCS is a 9 m-long test section with a 0.5 m-high and 0.4 m-wide rectangular cross section. It has glass sidewalls and acrylic lids along its entire length. The transparency of the test section makes it very convenient to set up light- or laser-based measuring instruments. A 0.2 m-deep trough below the test section is designed for holding sediments. Two 1 m-diameter stainless steel vertical cylindrical risers are connected to the two ends of the test section through honeycomb flow filters. One riser contains a hydraulically actuated piston for producing prescribed oscillatory flows in

the test channel, and the other is open to the atmosphere. Previous studies, e.g., Yuan and Madsen (2014), demonstrated that the WCS facility has the ability to produce specified oscillatory flow conditions with an extreme accuracy.

A Laser-based Bottom Profiler (LBP) was applied to measure the movable bottom profile in the test section. The laser units of the LBP produce two longitudinal laser lines on the movable bed, which are located symmetrically on both sides of the bed's lateral center line with half-width distance (200 mm) apart. Six side-viewing cameras capture these laser lines in a dark environment. A bottom profile can therefore be determined from the digital photos by tracing the peak local redness value. As an example, Figure 1c presents one laser-line photo of test Ta060 (see Table 2 for test conditions), and Figure 1b is the corresponding photo of the same section of the movable bed. Some preliminary tests demonstrated that the LBP's accuracy is up to $O(0.1)$ mm. For brevity, the readers are referred to Yuan et al. (2017a) for details about the LBP. When vortex ripples become quite large, e.g., the final equilibrium ripples of Te044 can be 177 mm tall, a significant amount of suspended sediment blocks the laser lines, so the bottom profile can only be measured after stopping the experiment (to let the sediments settle down). Nevertheless, when monitoring the initial stage of ripple development from a flat bed, sediment suspension is relatively weak, so the LBP measurements can be obtained without stopping the tests.

2.2. Test conditions

As simple approximations of wave-driven boundary layer flows, sinusoidal oscillatory flows were adopted in the first group of tests, which can be char-

acterized by a free-stream velocity

$$u_\infty(t) = U_{bm} \sin(\omega t) \quad (1)$$

where U_{bm} is the velocity amplitude, t is time and $\omega = 2\pi/T$ is the angular frequency with T being the flow period. According to Wikramanayake and Madsen (1994), rippled-bed condition under periodic sinusoidal flows is achieved if the following Shields parameter (ψ_{wmd}) criterion is satisfied

$$\psi_{cr} < \psi_{wmd} = \frac{\tau_{wmd}}{\rho(s-1)gd_{50}} = \frac{1}{2} \frac{f_{wmd}U_{bm}^2}{(s-1)gd_{50}} < 0.7 \quad (2)$$

where $g = 9.8 \text{ m/s}^2$ is the acceleration due to gravity, $\rho = 1000 \text{ kg/m}^3$ is water density, $s = 2.65$ is sediment specific density, τ_{wmd} is a characteristic maximum bottom shear stress, and the corresponding wave friction factor f_{wmd} is obtained following Humbyrd (2012) (an improvement of the widely-used Grant and Madsen (1979) model)

$$f_{wmd} = \exp[5.70(\frac{A_{bm}}{k_b})^{-0.101} - 7.46], \quad 10 < \frac{A_{bm}}{k_b} < 10^5 \quad (3)$$

where the roughness k_b is taken as $k_b = d_{50}$ and A_{bm} is the water excursion amplitude, which is calculated through $A_{bm} = U_{bm}/(2\pi/T)$. The critical Shields parameter ψ_{cr} for the incipient motion of sediment grains is calculated following Madsen and Wood (2002)

$$\psi_{cr} = \begin{cases} 0.1S_*^{-2/7} & S_* \leq 0.8 \\ 0.095S_*^{-2/3} + 0.056[1 - \exp(-S_*^{-3/4}/20)] & S_* > 0.8 \end{cases} \quad (4)$$

with

$$S_* = \frac{d_{50}}{4\nu} \sqrt{(s-1)gd_{50}} \quad (5)$$

where ν is the water kinematic viscosity, which is simply taken as 1×10^{-6} m²/s. In this study, the movable sand bed is made of well-sorted coarse sand with $d_{50} = 0.51$ mm and $\psi_{cr} = 0.034$, which had been adopted in the previous sheet-flow experiments (i.e., Yuan et al., 2017b). There is only one sediment grain size in this study, since 2-D ripples are easier to be formed with coarse sand (e.g., Pedocchi and García, 2009a), and our LBP system can only work with 2-D bedforms for measuring bottom profiles. Thus, the grain size effect was not investigated in this study. The selected sinusoidal flow conditions are presented in Table 2. These experiments cover a wide range of full-scale flow conditions ($Re_w = 5.77 \times 10^4$ to 1.39×10^6) with flow periods $T = 3.13 - 10.00$ s and $\psi_{wmd} = 0.064 - 0.695$. Based on the linear wave theory, these combinations of U_{bm} and T correspond to wave height from 0.51 m to 2.05 m in 5 m-deep waters. 6 of 16 flow conditions were repeated to verify the repeatability of the experiments and the number of repeats are indicated aside the flow conditions in Table 2. Prior to most tests, the sand bed was flattened, except for tests Td060 and Td075. These two tests were started with the rippled bed from a preceding test.

The wave nonlinearity was considered by adding a second-harmonic velocity to the sinusoidal oscillatory flows in the second group of tests. In this study, the ratio of second-harmonic velocity amplitude to the first-harmonic velocity amplitude was fixed as 1/4. Thus, the free-stream velocity is

$$u_{\infty}(t) = U_{bm} \sin(\omega t) + \frac{1}{4}U_{bm} \cos(2\omega t + \pi) \quad (6)$$

for skewed flows, and

$$u_{\infty}(t) = U_{bm} \sin(\omega t) + \frac{1}{4}U_{bm} \sin(2\omega t) \quad (7)$$

for asymmetric flows. Here we defined the positive direction as the onshore direction. The time series of the free-stream velocities are compared with the sinusoidal oscillation in Figure 2.

For easy comparisons, a skewed-flow test is paired with an asymmetric-flow test, which has the same U_{bm} and T , and six $U_{bm} - T$ conditions with periods from 4.17 s to 8.33 s and Shields parameters from 0.102 to 0.333 were chosen from those in Table 2, so totally 12 tests in this group were conducted and these tests are referred to as “nonlinear”-flow test hereafter (see Table 3). The ripples were first initiated from a flat bed using sinusoidal flows, and the two “nonlinear”-flow tests with same U_{bm} , were successively conducted with the obtained rippled bed. To guarantee the equilibrium stage had been reached, these “nonlinear”-flow tests were continued until no significant changes in both ripple size and shape can be observed, which usually took a few hours.

3. Ripple development

In this section, we present the observations regarding the development of vortex ripples under sinusoidal flows from a flat bed. For a few selected tests, the LBP was applied to record the evolution of bed profile. In the initial stage, the sediment suspension was not very strong, so the LBP system can be applied without stopping the flow within the first dozens of periods. Subsequently, the vortex-induced sediment suspension can block the laser lines, so we had to pause the test for a while (let the sediments to settle down) before taking LBP measurements. The time interval between pauses was about 50 – 100 periods. Two bed profiles following the two laser lines, $z_{b1}(x)$ and

$z_{b2}(x)$, were available for each measurement, so the bed's 2-dimensionality over the entire test section can be quantified by a global cross-correlation analysis of the two profiles. The global correlation coefficient γ_b is defined as

$$\gamma_b = \frac{L \cdot I(z_{b1}z_{b2}) - I(z_{b1}) \cdot I(z_{b2})}{\sqrt{[L \cdot I(z_{b1}^2) - I^2(z_{b1})][L \cdot I(z_{b2}^2) - I^2(z_{b2})]}} \quad (8)$$

where L is the length of the test section and

$$I(\xi) = \int_{x_0}^{x_L} \xi dx \quad (9)$$

represents the integral of variable ξ along the entire test section. x_0 and x_L are the two boundaries of the movable bed shown in Figure 1a. A perfect 2-dimensionality is represented by $\gamma_b = 1$. A zero-up-crossing technique was adopted to calculate the mean ripple dimension during the ripple development. The initial flat bed was taken as the zero datum for bed profile, and we picked the points where the profile up-crosses the zero datum. The average spacing between neighboring up-crossings was taken as the mean ripple length (λ_m) and the average of vertical highest-to-lowest distance between two successive up-crossings was taken as the mean ripple height (η_m). This analysis was separately applied to the two bottom profiles (z_{b1} and z_{b2}), which gives two sets of (η_m, λ_m). There is very little discrepancy between the two sets, so the average was taken as the final result. In addition, following a similar method proposed by Doucette and O'donoghue (2006), the averaged bed profile $z_b = (z_{b1} + z_{b2})/2$ was Fourier analyzed to give an amplitude spectrum, which will be used to illustrate the ripple development. In the following subsection, three typical situations based on the final bed condition are separately presented: 2-D ripples, sheet-flow limit and 3-D ripples.

3.1. 2-D ripples

Most of our tests ended with equilibrium 2-D periodic ripples (indicated in Table 2 as “2-D”). For these tests, the general ripple development processes agree well with the observations reported by some previous OWT studies, (e.g., O’Donoghue and Clubb, 2001). Here we briefly present our observations based on a typical test, Ta060 ($U_{bm} = 592$ mm/s, $T = 6.25$ s, $\lambda = 569$ mm, $\eta = 106$ mm). The development history is shown in Figure 3. In this test, the time interval of LBP measurements gradually increased from 5 periods to 100 periods, and totally 14 measurements were obtained. The mean ripple dimension calculated from each measurement was normalized by the final equilibrium value, λ and η , which will be discussed later in the next section. The whole development process took around 600 periods (~ 1 hour). Within a few periods since the beginning, small “ripple marks” (few millimeters in height), which occupied the full width of the tunnel, showed up very quickly along the entire movable bed. These ripple marks were quite 2-D, e.g., the global correlation coefficient was fairly large ($\gamma_b = 0.51$ at 5th period). During this stage, it can be argued that the sediment motion is dominated by bedload as the ripples are not steep enough for producing strong flow separation. In the next few dozens of periods, they grew in height and merged with each other, resulting in a transient 3-D rippled bed. The ripple crest lines became discontinuous in the lateral direction and the ripples were very non-uniform. As shown in Figure 3a, γ_b quickly decreased from 0.51 at 5th period to 0.16 at 40th period. This transient 3-D stage was relatively long and ended with the emergence of large 2-D ripples, e.g., γ_b increased from 0.16 at 40th period to 0.99 at 200th period. Once a good 2-dimensionality was established, the

ripples remained 2-D and kept growing (mostly in height) until equilibrium. For Ta060, ripple length reached equilibrium value at about the same time when a good 2-dimensionality was established (around 200th period), but the ripple height took much longer time to grow, e.g., the ripple height was 85% of the equilibrium value at 200th period and it took 100~200 more periods to reach equilibrium. This phenomenon was also observed for other tests with 2-D equilibrium ripples.

For test Ta060, the evolution of amplitude spectrum a_s as a function of T_d is presented in Figure 4a, where T_d is the number of period since the beginning. The x coordinate is A_{bm}/λ_s , where λ_s is the bedform wave length, and the y coordinate is T_d . The magnitude of amplitude spectrum is represented by the redness of the shade. To highlight the shifting of dominant mode with time, we present the normalized amplitude spectrum $a_s(T_d)/a_{rms}(T_d)$ in Figure 4b, where $a_{rms}(T_d)$ is the root-mean-square value of the bottom profile z_b at T_d . Thus, in the normalized figure, darker color indicates more concentrated energy distribution, which also means that the ripples are more uniform. As can be expected, since the ripple marks were fairly short in the first few periods, most of the spectrum energy was concentrated with $A_{bm}/\lambda_s > 2.0$ during the initial stage, i.e., $T_d < 40$ (see Figure 4b). From 40th to 200th period, i.e., the transient 3-D stage, the dominant mode shifted to around 1.04 and the spectrum became increasingly narrow. Note that $A_{bm}/\lambda_s = 1.04$ corresponds to the equilibrium ripple length of this test. The measurements suggest that there was no energy associated with this ripple length in the first 40 periods. This indicates that the final ripples were originated from the transient 3-D ripples stage, rather than the very

beginning. Once the spectrum was sufficiently concentrated around the final ripple length (i.e., after 200 periods), there was no more noticeable shifting of spectrum energy, only a gradual increasing of the amplitude (or ripple height).

3.2. Sheet-flow limit

In test Ta120 ($U_{bm} = 1184$ mm/s, $T = 6.25$ s and $\psi_{wmd} = 0.673$), which is fairly close to the sheet-flow limit ($\psi_{wmd} = 0.7$), no small ripple mark was observed during the initial stage. Instead, significant sediment motion, which is similar to that under sheet-flow conditions, was observed in the close vicinity of the flat movable bed. The sand bed remained quite smooth during the first 10 – 20 periods. Subsequently, large bedforms with length between 1000 – 2000 mm started to develop. These irregular bedforms were very 2-D, and the ones near the tunnel’s ends appeared earlier than those around the center, so they were probably produced and controlled by facility’s end effects. They became quite huge after 20–50 periods, and the flow separation generated on the lee-side of bedforms led to significant sediment suspension and transport. We stopped the test only after 0.2 hours (12 mins) because the bedform became very large and the suspended sediment clouds can even reach the top lid. As shown in Figure 5, the final bottom profile was very 2-D and irregular.

It is noted that test Ta120 is fairly close to the Experiment 11 documented in Pedocchi and García (2009b), in which $U_{bm} = 1000$ mm/s, $T = 6$ s, $d_{50} = 0.25$ mm and $\psi_{wmd} = 0.620$. Similar to our test, there was no small-scale ripple mark developed at the initial stage and large-scale bedforms were developed at the end of that test. From these two tests, it can be seen that

as flow approaching the sheet-flow limit, bottom shear stress over a flat sand bed becomes strong enough to prevent the development of the small ripple marks, which stops the subsequent ripple development. This, as suggested by Pedocchi and García (2009b), can be taken as a differentiator between sheet-flow and ripple-bed conditions.

3.3. 3-D ripples

For two test conditions, i.e., Tb030 and Tc040, the movable bed never became 2-D even after many hours (6.9 and 17.2 hours for Tc040 and Tb030, respectively). It is of interest to see the difference between these tests and the 2-D ripples cases. Tb030 is chosen to be a typical example in this subsection.

The development history for Tb030 ($T = 4.17$ s, $U_{bm} = 296$ mm/s and $\psi_{wmd} = 0.073$) is presented in Figure 6a to 6c. Four typical bottom profiles (z_b) are shown in Figure 6d to 6g. The color bars represent the local $\gamma_b(x)$ which is the correlation coefficient for a piece of 100-mm-long bottom profile centered at x . At the beginning, e.g., around 10th period, the whole test section was covered by small ripple marks, which is similar to those tests with final 2-D ripples (Figure 6d). However, instead of quickly becoming 3-D, the majority of ripple marks remained fairly 2-D and grew in size (up to $\lambda_m = 160$ mm and $\eta_m = 20$ mm). This stage of ripple development (defined as stage A in Figure 6) continued for about 2000 periods. A typical bottom profile during this stage (at the 800th period) is shown in Figure 6e. It can be seen that most of the test section ($3000 \text{ mm} \leq x \leq 9000 \text{ mm}$ in Figure 6e) was occupied by those small ripples, which are quite uniform and 2-D (local γ_b is very close to 1). Transient 3-D ripples were only observed for a small region near left end of the test section ($0 \leq x \leq 3000 \text{ mm}$ in Figure

6e). These 3-D ripples were much larger than the 2-D ripples ($\eta_{m,3D} = 45$ mm vs. $\eta_{m,2D} = 22$ mm and $\lambda_{m,3D} = 250$ mm vs. $\lambda_{m,2D} = 120$ mm). They slowly grew in size, and the 3-D zone also gradually extended into the 2-D region. Since the number of small 2-D ripples (~ 50) was much larger than the number of 3-D ripples (~ 10) during stage A, the average ripple dimensions were very close to the values of small 2-D ripples, until the 3-D zone became sufficiently large. This explains the nearly constant values for η_m and λ_m during stage A. The transient 3-D ripples gradually extended to the whole test section (e.g., the bottom profile at 3000th period shown in Figure 6f), and then slowly grew in dimension while still maintained their 3-dimensionality, i.e., the global γ_b is generally less than 0.4. After 13000 periods, it seems that λ_m converged to 230 mm and η_m converged to 40 mm, while the global γ_b fluctuated around only 0.4. Therefore, it can be concluded that an equilibrium stage with 3-D ripples was achieved.

The evolution of amplitude spectrum is shown in Figure 4c and 4d for the absolute $a_s(T_d)$ and normalized values $a_s(T_d)/a_{rms}(T_d)$, respectively. The coexistence of small 2-D ripples and large 3-D ripples in stage A is clearly revealed by the spectrums, i.e., two significant modes ($A_{bm}/\lambda_s \sim 0.6$ and 1.7) were observed in the first 2000th-4000th periods (two circles in figure 4c and 4d). The short-wave-length mode gradually disappeared until roughly 4000th period, so the spectrum became narrower. The remaining mode ($A_{bm}/\lambda_s \sim 0.6$) became dominant till the end of this test.

3.4. Planform geometry

As introduced in section 1, many criteria had been developed for determining whether the equilibrium ripple is 2-D or 3-D. Since some of our tests

gave 3-D ripples, it is of interest to see if these criteria agree with our observations. Almost all these criteria were developed based on: (i) flows with large A_{bm} and U_{bm} tend to form 3-D ripples because the coherent vortex can contain more 3-D small-scale turbulent structures; (ii) ripples formed in coarser sediments tend to be more 2-D because the larger inertia of sediment grains supersedes the effect of small 3-D turbulence. Note that for large grain size (like $d_{50} = 0.51$ mm in our study) and realistic wave periods, A_{bm}/d_{50} can not be very large, otherwise a sheet-flow condition will occur. Among those criteria, the one recently proposed by Pedocchi and García (2009a) is the most comprehensive one, so it was chosen to compare with our observations. Their criterion for the occurrence of 3-D ripples is

$$Re_p < 0.06 Re_w^{0.5} \quad (10)$$

where $Re_p = \sqrt{(s-1)gd_{50}}d_{50}/\nu$ is the sediment Reynolds number and $Re_w = U_{bm}A_{bm}/\nu$ is a wave Reynolds number. Re_p reflects whether the sediment particles are large and heavy while Re_w represents the oscillatory boundary layer flow. Flows with large Re_w usually have thicker boundary layer, in which more significant (and 3-D) turbulent motions can exist. Thus, the ripples tend to be 2-D either if the sediment particles are large and heavy (large Re_p) or the flow is sufficiently weak (small Re_w). For our tests ($Re_p \approx 46$), Eq.(10) gives the lower limit for 3-D ripples: $Re_w = 5.8 \times 10^5$. Comparing this threshold with Re_w shown in Table 2, only three 2-D cases (3/13) are wrongly predicted and they are quite close to the threshold.

However, the predictor fails to capture the two 3-D tests. These two tests are the ones with smallest A_{bm} , so compared to the other tests they should have better chances to be 2-D according to the criterion. We believe that

the facility effect may play a role. As demonstrated by Yuan and Madsen (2014), for oscillatory flows in a water tunnel, the flow near the corner is controlled by both bottom and sidewall boundary layers while the near-bed flow far away from the corner is only controlled by the bottom boundary layer. For a rough bottom this inhomogeneity will produce an upward drift along the sidewalls and a downward drift along the vertical centerline (Fujita et al., 1989), as the red lines shown in Figure 7. This secondary transverse flow can be considered as a weak vortex with a length scale $L_t = b/2 = 200$ mm in the spanwise direction. If the ripple length is close to L_t , the ripple height can be quite sizable (30-50 mm), leading to significant lee-side flow separations and coherent vortices. In such circumstances, the length scales of coherent vortices (scaled with ripple length λ) and transverse flow L_t become similar, so their mutual interaction determines that the flow and the suspended sediment motion are significantly 3-dimensional. Even if the bedform is 2-D, such a mechanism can break 2-D ripples into 3-D ones. Among all tests, the two 3-D cases (final $\lambda_m = 242$ mm and 202 mm) have ripple lengths closest to 200 mm, also the transient 3-D ripples for test Ta060 (a 2-D case) has the strongest 3-dimensionality when the mean ripple length is 200-300 mm (see Figure 3a and b). These evidences support the hypothesis that the facility's effect is the reason for the two 3-D tests. If the ripple length becomes smaller ($\lambda \ll L_t$), there will be a larger separation between the length scales of transverse flow and coherent vortices. Also, a smaller ripple height associated with a smaller ripple length will lead to less suspended sediment transport for the transverse flow to be influential, so the bedform can remain fairly 2-D. This explains the 2-dimensionality of small ripple

marks during the initial stage of ripple development, as well as the very 2-D transient ripples during stage A of Tb030. If the ripple length becomes larger ($\lambda \gg L_t$), e.g., all equilibrium 2-D ripples, the associated larger ripple height leads to a stronger coherent vortex motion, which supersedes the effect of the weak transverse flows, so a 2-D bed can be stable.

The tunnel width effect on planform geometry is also worth discussing. To produce full-scale prototype flows, the excursion amplitude A_{bm} in this study are mostly larger than the tunnel width $b = 400$ mm. This, to some extent, can limit the development of 3-dimensionality for both flows and bedforms (e.g., Pedocchi and García, 2009a; Cummings et al., 2009), so an immediate question is whether the 2-dimensionality in most of our tests is merely due to facility's limited width. In a field study by Traykovski et al. (1999), 2-D vortex ripples, which are about 900 mm long and 140 mm tall, were observed under field wave condition $A_{0,1/3} \approx 700$ mm and $T_s \approx 10$ s (see yearday 251 of their Figure 5) where $A_{0,1/3}$ is the significant wave excursion amplitude and T_s is a characteristics wave period based on near-bed flow velocity spectrum. This field wave condition is comparable to Te044 ($A_{bm} = 690$ mm and $T = 10.0$ s) in this study, so the 2-D ripples formed in test Te044 should be realistic. For the rest 12 tests with 2-D ripples, only four tests have A_{bm} larger than that of Te044, and the largest A_{bm} (982 mm for Ta100) is not too far from 690 mm. Therefore, it is reasonable to believe that the limited tunnel width should not be a dominant factor for determining planform geometry in our study, and the 2-D ripples obtained in this study are meaningful.

4. Equilibrium 2-D ripples under sinusoidal flows

In this section, we present the geometric characteristics of equilibrium 2-D ripples generated by sinusoidal flows. We start with some brief results on ripple dimensions. A representative ripple profile, which is the ensemble average of a ripple train, is then introduced to investigate the overall ripple shape. Finally, the roundness of ripple crest and the maximum local slope on the ripple flank are investigated to reveal some detailed characteristics of vortex ripples.

4.1. Ripple Dimension

For most tests, about 10–20 periodic 2-D ripples were developed from the 9-m-long movable bed. To estimate the equilibrium ripple length λ , we measured the distance between two adjacent ripples' crests, i.e., λ_i , in Figure 8a, and taken the average value of λ_i as the final measurement with standard deviation σ_λ indicating the experimental uncertainty. The equilibrium ripple height η and its variability σ_η were obtained based on the representative ripple profile (see next subsection). Due to the end effect, some imperfect ripples near the two ends were manually excluded in the analysis. The measured equilibrium ripple dimension is shown in Table 2. The dimensions of the two 3-D tests are the mean ripple dimension, η_m and λ_m , of the final bottom profile from the zero-up-crossing analysis introduced in section 3. The relative standard deviations defined as $\sigma_\lambda^* = \sigma_\lambda/\lambda$ and $\sigma_\eta^* = \sigma_\eta/\eta$ are presented in the bracket aside (as a percentage) the corresponding dimension measurements in Table 2. It is seen that for 2-D cases, σ_λ^* and σ_η^* are 5% and 10% on average, respectively, indicating that the ripples are very uniform.

The ripple length is generally scaled with the excursion amplitude A_{bm} , i.e., $A_{bm}/\lambda = 0.7 - 1.3$ and the ripple steepness η/λ varies within a small range from 0.15 to 0.20, which agrees with the vortex ripples found in field and other full-scale OWT experiments (e.g., Traykovski et al., 1999; O’Donoghue et al., 2006). Among many predictors for ripple dimension, here we simply choose the Grant and Madsen (1982) predictor for a brief model-data comparison, i.e.,

$$\frac{\eta}{A_{bm}} = \begin{cases} 0.22(\psi_{wmd}/\psi_{cr})^{-0.16}, & \psi_{wmd}/\psi_{cr} \leq 1.8S_*^2 \\ 0.48S_*^{0.6}(\psi_{wmd}/\psi_{cr})^{-1.5}, & \psi_{wmd}/\psi_{cr} > 1.8S_*^2 \end{cases} \quad (11)$$

and

$$\frac{\eta}{\lambda} = \begin{cases} 0.16(\psi_{wmd}/\psi_{cr})^{-0.04}, & \psi_{wmd}/\psi_{cr} \leq 1.8S_*^2 \\ 0.28S_*^{0.6}(\psi_{wmd}/\psi_{cr})^{-1.0}, & \psi_{wmd}/\psi_{cr} > 1.8S_*^2 \end{cases} \quad (12)$$

where S_* is a dimensionless sediment parameter defined in Eq.(5). Our measurements are plotted against the predictions in Figure 9. Overall speaking, this model slightly under-predicts the ripple height by 13% and over-predicts the ripple length by 9%, especially for large ripples, but the deviation is usually smaller than 20%. This agreement demonstrates that the ripples obtained in our experiments indeed achieved the equilibrium stage. The circles in Figure 9 are the two 3-D cases (Tb030 and Tc040), whose dimensions still agree quite well with the predictions. It should be noted that the measured ripple steepness is generally larger than the prediction. This is probably because the A_{bm}/d_{50} value in our study is smaller than other tests involving fine and medium sands (Note that the model was calibrated based on tests with a variety of grain sizes). As A_{bm}/d_{50} increases, the ripple steepness will decrease due to wash-off processes and finally enter the sheet-flow regime.

For cases Td045 and Td075, which were started from a preceding rippled bed (instead of a flat sand bed), the dimensions of equilibrium ripples agree fairly well with the predictions (indicated by the triangles in Figure 9). This supports the argument proposed by Doucette and O’donoghue (2006) that the initial bed configuration (flat or pre-rippled) may not influence the final equilibrium bed configuration.

4.2. Equilibrium ripple profile

For tests with uniform 2-D ripple trains, it is meaningful to ensemble average the individual ripples into a representative ripple profile. The ensemble-averaging was carried out as follows. For a measured bottom profile (e.g., Figure 8a), we first located each ripple crest and cut out a piece of profile with length 1.2λ (λ is pre-determined in section 4.1) around it. These pieces of profiles were then collocated by putting the crests together, (e.g., Figure 8b) and ensemble averaged. In such a way, the shape of ripple crest can be preserved as much as possible. As can be expected, the ensemble-averaged profile is usually very symmetric regarding the ripple crest. Therefore, we further averaged the two half-ripples, so the final representative ripple profile consists of two symmetric halves regarding the joint (ripple crest). The representative ripple profile $z_R(x_R)$ for a typical test (Ta040) is shown in Figure 8c, with a standard deviation (the grey zone) $\sigma_R(x_R)$ indicating the variability, where x_R is a local longitudinal coordinate with $x_R = 0$ at the ripple crest. This standard deviation, which comes from the ensemble-averaging, is usually a few percentage of the ripple height. The equilibrium ripple height η was taken as the vertical distance from the crest to the trough, as indicated in Figure 8c. The variability of η is just $\sigma_R(x_R)$ at ripple troughs, since σ_R

is forced to be zero at the crest.

To better illustrate the difference of ripple shapes among various flow conditions, we normalized the representative ripple profiles by

$$\begin{aligned} x_* &= x_R/\lambda_R \\ z_* &= z_R/\eta \end{aligned} \tag{13}$$

where λ_R (see Figure 8c) is the horizontal distance between the two troughs of the representative ripple profile. Note that there is a negligible difference ($< 1\%$) between λ_R and λ . As introduced in section 1, two conceptual ripple profiles for equilibrium 2-D vortex ripples were usually adopted in modeling sediment transport: the sinusoidal profile and the one proposed by Du Toit and Sleath (1981) (DS81 hereafter). The sinusoidal profile can be normalized as

$$z_* = \frac{1}{2} \cos(2\pi x_*), \quad |x_*| \leq \frac{1}{2} \tag{14}$$

which has symmetric crest and trough. The normalized DS81 profile is

$$\begin{cases} x_* = \frac{\zeta}{\lambda} - \frac{1}{2} \frac{\eta}{\lambda} \sin(2\pi x_*) \\ z_* = \frac{1}{2} \cos(2\pi \frac{\zeta}{\lambda}) \end{cases} \quad \zeta \leq \frac{\lambda}{2} \tag{15}$$

which has a relatively shaper crest and flatter trough than the sinusoidal profile. Note that the DS81 profile is quite close to the parabolic profile proposed by Fredsøe and Deigaard (1992), except for a small difference (5%–15% of z_*) near the crest.

We compare the measured profiles with the two conceptual profiles in Figure 10. Ta045 is omitted here since it is quite close to both Ta040 and Ta050. The first thing to notice is that both two conceptual profiles cannot well approximate all tests, and it is interesting to see that the measurements (red

solid lines) are always between the sinusoidal (dash-dotted lines) and DS81 (dashed lines) profiles. Comparing Ta-series tests (from Ta030 to Ta100), it can be clearly seen that as the flow condition (represented by ψ_{wmd}) becomes stronger, the ripple flanks become increasingly concaved upward and the ripple crest becomes more rounded. As a result, only the test with the lowest ψ_{wmd} , Ta030 ($\psi_{wmd} = 0.062$), has a ripple profile closer to the DS81 profile, while ripple profiles for the remaining tests can be approximated by sinusoidal profiles, except that the actual ripple crests are slightly sharper. We also note that the ripple shape seems to be less sinusoidal for shorter flow period. The ripple profiles of tests Tb060 and Tb075 ($T = 4.17$ s) deviate quite considerably from the sinusoidal profile. Notice that their ψ_{wmd} (0.228 and 0.334) is above that for Ta060 ($\psi_{wmd} = 0.203$), and therefore would imply quite sinusoidal profiles if the period was 6.25 s. This suggests that ψ_{wmd} is not the only parameter controlling ripple shapes.

To quantitatively illustrate the similarity between the measured and those conceptual ripple profiles, we calculate the root-mean-square (rms) error ε , which is defined as

$$\varepsilon = \sqrt{\int_{-1/2}^{1/2} (z_{*m}(x_*) - z_{*p}(x_*))^2 dx_*} \quad (16)$$

where z_{*m} and z_{*p} represent measured and conceptual profiles, respectively. We introduce a similarity index

$$\beta_\varepsilon = \frac{\varepsilon_{DS}}{\varepsilon_{DS} + \varepsilon_{sine}} \quad (17)$$

where ε_{DS} and ε_{sine} are the rms error for DS81 and sinusoidal profiles, respectively. β_ε can vary from 0.0 for exact DS81 profile to 1.0 for exact sinusoidal

profile. The results of β_ε are plotted against ψ_{wmd} in Figure 11a. A trend given by measurements of Ta-series tests (open circles) shows that the ripple shape evolves from closer to DS81 profile ($\beta_\varepsilon < 0.5$) for $\psi_{wmd} = 0.062$ to quite sinusoidal ($\beta_\varepsilon = 0.93$) for $\psi_{wmd} = 0.204$. As ψ_{wmd} further increases, β_ε slightly decreases to around 0.80 (Ta100). The two points corresponding to two 4.17-s tests are below those with longer periods, which follows the aforementioned period effect.

It can be argued that the shape of vortex ripple is controlled by the coherent vortex motions. Since the size of the lee-side vortex is scaled with the free-stream excursion amplitude A_{bm} , the ratio, A_{bm}/λ , can be taken as a parameter representing the influencing range of a coherent vortex. A larger A_{bm}/λ indicates that the vortex can affect a larger area of the ripple flank. In our tests, A_{bm}/λ varies substantially between 0.74 to 1.22. Using the size of sediment cloud entrained by the lee-side vortex as a visualization, we observed that in test Ta080 ($A_{bm}/\lambda=1.11$), the entire region from crest to trough was actively controlled by the lee-side vortex, while for Ta040 ($A_{bm}/\lambda=0.86$), only the region near the crest was affected due to a much weaker vortex (see Figure 12). Therefore, we plot β_ε against A_{bm}/λ in Figure 11b. The data points nicely form a trend that β_ε increases with A_{bm}/λ , and there is no obvious data stratification due to flow period. We can take A_{bm}/λ as the relative length of vortex ripple, i.e., larger A_{bm}/λ indicates “shorter” ripples. The results therefore suggest that vortex ripple becomes increasingly sinusoidal as they become “shorter”, which allows the coherent vortex to control a larger portion of the ripple flank. In our tests, larger A_{bm}/λ value corresponds to larger Shields parameter ψ_{wmd} (for a given flow

period), which is also suggested by most dimension predictors (e.g., Grant and Madsen, 1982; Pedocchi and García, 2009a). For waves over coarse-sand bed, large value of ψ_{wmd} (0.2–0.3) and wave period around 6–8 s correspond to Re_w of $O(\sim 10^5)$, e.g., Ta080 and Td060 in our study. Therefore, it can be argued that full-scale vortex ripples developed from coarse-sand bed can be better described by sinusoidal profiles.

4.3. The roundness of ripple crest

The roundness of ripple crest controls the vortex development and shedding, and therefore deserves some detailed investigations. Some previous OWT studies (e.g., Pedocchi and García, 2009a) already pointed out that full-scale vortex ripples can have quite rounded crests. This is clearly different from the impression that vortex ripples are sharp-crested, which came from small-scale flume or oscillating tray experiments (e.g., Du Toit and Sleath, 1981). It should be pointed out that the ripple crest keeps deforming within one flow period, while the measurements of equilibrium bed profile were taken after stopping the tests, so the results should be interpreted as period-averaged results.

Here we simply use the radius of the osculating circle, i.e., inverse of the curvature (see illustration in Figure 13a), to quantify the roundness of a given ripple profile, which is defined as

$$R(x) = \frac{(1 + z'_b(x)^2)^{\frac{3}{2}}}{|z''_b(x)|} \quad (18)$$

where z'_b and z''_b are the first- and second-order x -gradient of the ripple profile $z_b(x)$, respectively, and larger R means the local profile is more rounded.

Instead of using the representative ripple profile z_R , here the analysis is directly based on the original bottom profile z_b because the ensemble-averaging may round the ripple crests. The roundness at ripple crests R_c was evaluated ripple-by-ripple for the whole bottom profile. The average value was taken as the final measurement with a standard deviation representing the uncertainty. The results are plotted against ψ_{wmd} in Figure 13b. The data points form a quite clearly trend that R_c increases with ψ_{wmd} , and there is not much separation for tests with different periods. This can be seen by comparing the two cases Ta040 ($\psi_{wmd} = 0.102$) and Te044 ($\psi_{wmd} = 0.103$), which have huge difference in dimension but fairly similar R_c ($\lambda = 455$ mm, $R_c = 70$ mm for Ta040 vs. $\lambda = 833$ mm, $R_c = 60$ mm for Te044). Having close R_c indicates similar shape of the ripple crest. The parameter ψ_{wmd} can be taken as a representative parameter describing the local flow around a ripple crest. Thus, our measurements suggest that the shape of ripple crest is mostly controlled by the local flow conditions.

R_c value increases with ripple size for self-similar ripples, so a normalized value, R_c/η , is also introduced here as another parameter to describe the sharpness of the ripple crest. As shown in Figure 13c, the normalized value clearly decreases with flow period for a given ψ_{wmd} , which is simply because larger flow period T leads to larger ripples. This suggests that ripples formed in long-period flows are generally “sharper” than those formed in short-period flows, e.g., comparing Ta040 and Te044 in Figure 10.

4.4. *Maximum local slope on the ripple flank*

Since the local slope of the ripple profile is zero at the trough and the crest, a point with maximum value of local slope should occur on the ripple flank

(see Figure 13a). This maximum slope $\beta_{s,max}$ should not exceed a certain threshold value, since avalanching or an infinite sediment transport rate will occur for a very large local slope. For a train of equilibrium ripples developed under sinusoidal oscillatory flows, $\beta_{s,max}$ was evaluated ripple-by-ripple on both two ripple flanks, and we take the average as the final measurements. As shown in Figure 14a, there is a clear decreasing trend of $\beta_{s,max}$ from more than 35° for $\psi_{wmd} = 0.064$, which is very close to the critical value of incipient motion, to around 28° - 30° for $\psi_{wmd} = 0.490$, which indicates a quite intense flow condition. No clear period dependency is observed, due to the fairly significant (1° - 2°) standard deviation (error bars in Figure 14a). It is noted that $\beta_{s,max} = 35.2^\circ$ for Ta030 is very close to the lower static angle of repose ($\sim 36^\circ$) proposed by Cheng and Zhao (2017) for the coarse sand adopted in our study. This is because in low ψ_{wmd} flows, the vortex's ability for suspending sediments is quite weak. The majority of suspended sediment grains during the one half-period are therefore deposited back onto the ripple surface around the moment of flow reversal. Thus, the formed ripple flank should have a maximum slope close to the lower static angle of repose. As the flow becomes energetic, the wash-off processes due to large ψ_{wmd} flattens the ripples, making, η/λ and hence $\beta_{s,max}$ smaller, e.g., $\beta_{s,max}$ decreases to 28° for Ta100.

It is also of interest to document the location of maximum local slope. Here we present the longitudinal distance, $L_{\beta,max}$, from the ripple crest to the location of $\beta_{s,max}$. We further normalize $L_{\beta,max}$, i.e., $\gamma_{\beta,max} = L_{\beta,max}/\lambda$, so $\gamma_{\beta,max} = 0, 0.25$ and 0.5 correspond to ripple crest, midpoint between crest and trough and ripple trough, respectively. The results are shown in

Figure 14b. Similar to $\beta_{s,max}$, $L_{\beta,max}$ is directly measured ripple-by-ripple, so a standard deviation is also obtained for quantifying the experimental uncertainty (the error bars in Figure 14b). It is noted that the ripple profile is quite straight around the location of $\beta_{s,max}$, so determined $\gamma_{\beta,max}$ has quite a significant uncertainty. Nevertheless, it is still clear that $\gamma_{\beta,max}$ varies closely around 0.25 (± 0.05) regardless of the flow conditions. This implies that for all the obtained ripple profiles, the maximum local slope most likely appears at the midpoint between the ripple trough and crest, which is also the case for the conceptual sinusoidal profile.

5. Effect of wave nonlinearity on ripple geometry

Significant changes of ripple geometry due to wave nonlinearity were observed in all our experiments. Two examples of the ripples under skewed flows and asymmetric flows (Ta060S and Ta060A) are shown in Figure 15a and b, respectively. It can be clearly seen that skewness makes ripples onshore-leaning. This phenomenon agrees with other experiments involving skewed flows (e.g., van der Werf et al., 2007). Asymmetric flows, however, make ripples' crests sharper and troughs flatter. Small humps (a few millimeter in height) were usually observed at the long troughs of asymmetric-flow-generated ripples. In this section, the effect of wave nonlinearity on ripple shape is investigated by comparing “nonlinear”-flow and sinusoidal-flow tests in terms of ripple dimension, normalized ripple profiles, crest roundness and maximum slopes on two ripple flanks.

5.1. *Effect on ripple dimension*

Ripple dimension of the “nonlinear”-flow tests was determined as follows. The ripple length was still taken as the average spacing of two adjacent ripple crests. Ripple height was the vertical highest-lowest distance of the representative ripple profile. Two estimates of ripple height were obtained for the two half-ripples on both sides of the ripple crest, and the average value was taken as the final measurement. As shown in Table 3, the standard deviation of ripple dimension is relatively small, i.e., an average of 3.7% for ripple length and an average of 4.7% for ripple height, indicating a good periodicity of the rippled bed. Figure 16 compares the ripple dimensions of “nonlinear”-flow tests with those of corresponding sinusoidal-flow tests. As shown in Figure 16a, both asymmetry and skewness decrease ripple height, and the effect is more prominent for larger ripples (up to 19.9% of reduction). However, the two nonlinear features have different effects on the ripple length. Flow asymmetry increases the ripple length by 8.1% on average, while flow skewness reduces the ripple length by about 11.0% as shown in Figure 16b. In terms of ripple steepness, η/λ , the skewness’s effect is negligible since it reduces both η and λ , but flow asymmetry will reduce steepness by 10.9%-19.3%.

5.2. *Effect on equilibrium ripple profile*

The equilibrium ripple profiles were ensemble averaged and normalized following Eq.(13), so they can be easily compared with the ripple profiles generated by the corresponding sinusoidal flows (see Figure 17). The effect of wave nonlinearity on ripple shape can be easily visualized through this comparison. The left column of Figure 17 shows the six asymmetric-flow tests.

The red solid lines are always below the black dashed lines, which confirms our visual observations that asymmetry makes the ripple have sharp crests and flat troughs. The right column of Figure 17 presents the six skewed-flow tests. It can be clearly seen that the ripple crests are generally shifted to the right (onshore direction), and the right (onshore) flanks are steeper than the left (offshore) flanks, which reflects the onshore-leaning feature as shown in Figure 15a.

Two ripple shape factors,

$$Asy = 1 - 2 \cdot \frac{\lambda_p}{\lambda} \quad (19)$$

and

$$Skw = 2 \cdot \frac{\eta_p}{\eta} - 1 \quad (20)$$

are introduced to quantitatively illustrate the changes in ripple profiles (see Figure 18 for definition of parameters). Both Asy and Skw are zero for a sinusoidal profile. Asy is positive (negative) for onshore- (offshore-) leaning ripples, whereas $Skw > 0$ indicates the ripple shape is skewed (sharp crest and flat trough). Figure 18 presents the values of Asy and Skw for the “nonlinear”-flow tests, as well as the corresponding sinusoidal-flow tests. As can be expected, sinusoidal-flow-generated ripples have very little asymmetry (average Asy is 0.0018), and some of them have a slight skewness (up to about 0.06), which is due to the scale effect as discussed in section 4, i.e., ripples have sharp crests and flat troughs for flows with low Shields parameter (Ta040). For asymmetric-flow-generated ripples (red squares), the skewness of ripple profiles increase dramatically, giving an average of $Skw = 0.0990$.

Asy values for these ripples fall on same level (nearly zero) as the sinusoidal-flow-generated ripples. The onshore-leaning of skewed-flow-generated ripples (blue triangles) is clearly revealed by the values of Asy , i.e., Asy ranges from 0.05-0.15 for these six cases. Meanwhile, these ripples have similar crests and troughs, giving very small absolute Skw values.

In figure 18, the three data clouds are separated clearly, indicating a significant and consistent changing in ripple shape for different wave nonlinear features. Our measurements suggest that the skewed flows make ripples become asymmetric while asymmetric flows make ripples become skewed. In the coastal regions, shoaling waves contain both skewness and asymmetry. Therefore, more research effort should be spent on studying the ripple profiles under the mixed effect of waves skewness and asymmetry.

5.3. Effect on crest roundness and maximum slope along ripple flanks

In this section, crest roundness and maximum slope along the flanks are investigated following the same methods introduced in section 4.3 and 4.4. Figure 19 compares the R_c values for both asymmetric-flow-generated ripples (red squares) and skewed-flow-generated ripples (blue triangles) with sinusoidal-flow-generated ripples. A general decreasing of R_c is observed for both two features of wave nonlinearity. This decreasing is more significant for asymmetric-flow tests (-17% on average), of which the crests become sharper. For skewed-flow-generated ripples, the onshore-leaning shape has little effect on the crest roundness, so only a slight changing of R_c (-7% on average) is observed.

The two ripple flanks under “nonlinear” flows are no longer symmetric regarding the ripple crests, so the maximum bottom slope $\beta_{s,max}$ is evaluated

for both ripple flanks. The measurements are compared with the $\beta_{s,max}$ from the corresponding sinusoidal-flow tests. As shown in Figure 20, a quite noticeable decrease (up to 5° - 10°) of $\beta_{s,max}$ along the offshore flanks of skewed-flow-generated ripples is observed. The flow skewness elongates the offshore flank and makes it much gentler, leading to this dramatic decreasing in $\beta_{s,max}$. Except for this significant change, $\beta_{s,max}$ remains unchanged or slightly decreases for the rest cases. As argued in section 4.4, $\beta_{s,max}$ has an upper limit that is controlled by sediments' angle of repose and ripple steepness. These arguments are still applicable for "nonlinear"-flow tests, so $\beta_{s,max}$ can only be reduced.

6. Discussions and Conclusions

A full-scale experimental study of detailed ripple geometry was conducted in an oscillatory water tunnel. Two groups of tests, i.e., sinusoidal-flow tests and "nonlinear"-flow tests, were involved in this study with $T = 3 - 10$ s and $\psi_{wmd} = 0.064 - 0.673$. The wave nonlinearity effect was considered by adding a second harmonic to the sinusoidal oscillatory flow, and both wave skewness and asymmetry were investigated. The wave Reynolds number Re_w ranges from 5.77×10^4 to 1.39×10^6 , so most flow conditions can be regarded as full-scale. Using well-sorted coarse sand ($d_{50} = 0.51$ mm), 2-D equilibrium ripples were generated by sinusoidal flows from a flat sand bed after $O(100 - 1000)$ flow periods in most cases. The development of 2-D ripples agrees well with previous studies, i.e., it follows: "flat bottom" \rightarrow "2-D ripple marks" \rightarrow "3-D transient ripples" \rightarrow "2-D equilibrium ripples". There are two cases ended with 3-D equilibrium ripples, which have smallest A_{bm} . They should be 2-D

according to existing criteria, and we think the secondary transverse flow due to facility effect is a possible reason for the 3-dimensionality.

For sinusoidal-flow-formed ripples, the ripple dimensions agree with existing equilibrium dimension predictors. The ripple steepness is slightly underestimated probably because the A_{bm}/d_{50} for our cases are limited to low values. For each flow condition, 10-20 individual ripples were ensemble averaged and normalized into a representative ripple profile, which is further compared with existing conceptual profiles. Neither the sinusoidal profile nor the DS81 profile can always well approximate our measurements. The general trend is that the ripples become increasingly sinusoidal for high Shields parameter cases, while shorter flow period makes the ripple less sinusoidal. Additionally, since ripple shape is closely controlled by the coherent vortex, whose size is usually scaled with A_{bm} , more sinusoidal ripples were found for cases with larger value of A_{bm}/λ . Benefiting from high-quality measurements of ripple profiles, detailed geometrical characteristics, i.e., crest roundness and maximum slope along flanks, were examined. Generally speaking, ripple crests become more rounded as Shields parameter increases, which agrees with the observations reported by Pedocchi and García (2009b). The maximum slope along ripple flanks also decreases with Shields parameter because energetic flows can flatten the ripples. It is generally accepted that more significant flow separation occurs for ripple with sharper crest and steeper ripple flank. This flow separation induced vortex can affect both the amplitude and intra-period variation of flow resistance (e.g., Nielsen, 1988; Barr et al., 2004; Yuan and Wang, 2018). Our study suggests that full-scale coarse-sand ripples are not self-similar for different flow conditions, so an appropriate ripple

shape should be adopted in modeling both fluid mechanics and sediment transport. For instance, to model sediment transport over coarse-sand ripples with full-scale flow conditions, adopting sinusoidal ripple profile may increase the geophysical relevance.

The flow nonlinearity has a significant effect on ripple shape. Flow asymmetry makes ripples longer while skewness makes ripple shorter. Ripple height decreases due to both nonlinear features. Nevertheless, the variation of ripple dimension due to flow nonlinearity is generally less than 20%. In addition, flow skewness can make ripples onshore-leaning, which agrees with many existing observations, while asymmetric flows increase the skewness of ripple profiles, forming ripples with sharper crests and flatter troughs. The overall changes in ripple shape can also be reflected in the crest roundness and maximum slope along ripple flanks.

In the open literature, both of the two flow nonlinearities were considered more or less in modeling sediment transport. To the authors' knowledge, the imbalance of sediment transport under the two halves of a wave period is modeled by only considering how nonlinearity differentiates the half-period flows, while little attention is paid to the ripple-shape effect. Under skewed-flow conditions, ripples' onshore flanks are steeper than the offshore flanks, so flow separation and development of coherent vortex during the onshore half-period are more significant compared to those under the offshore half-period. Following the "grab-and-dump" concept, the asymmetric ripple shape will produce a net offshore transport rate, because the onshore-side coherent vortex can grab more sediment grains from the onshore flank and dump them on the offshore flank. This ripple-shape-induced net transport is on top of the

pure flow skewness effect. It is unclear how the effect of flow asymmetry on ripple shape (i.e., making ripples skewed) can affect net sediment transport rate, but at least we can believe that the relatively sharper ripple crests can enhance flow separation and therefore improve sediment entrainment and suspended-load transport rate.

A very recent work of Wang and Yuan (2018) showed that a finite bottom slope can make ripple upslope- (or usually onshore-) leaning. In field conditions, both wave nonlinearity features (skewness and asymmetry) and bottom slope co-exist. It is of interest to see how these factors together determine ripple shape. To this end, additional experiments with combined factors, e.g., “nonlinear” flows over sloping bottom, are required. The necessity comes from the fact that coastal sediment transport is a very nonlinear process, so simply superimposing individual effects is questionable. Additionally, since only coarse sand was involved in this study, our conclusions are limited to a relatively small dynamic range of A_{bm}/d_{50} . Finer sand with less inertia may respond to the flow motion in a different way (e.g., forming 3-D ripples), so further research should address the sediment grain size effect.

Acknowledgments

The authors gratefully acknowledge the financial support from the Tier-1 research project funded by the Ministry Of Education of Singapore (WBS: R-302-000-126-112).

References

- Bagnold, R.A., Taylor, G., 1946. Motion of waves in shallow water. interaction between waves and sand bottoms. *Proceedings of the Royal Society of London. Series A. Mathematical and Physical Sciences* 187, 1–18.
- Barr, B.C., Slinn, D.N., Pierro, T., Winters, K.B., 2004. Numerical simulation of turbulent, oscillatory flow over sand ripples. *Journal of Geophysical Research: Oceans* 109. doi:10.1029/2002JC001709.
- Blondeaux, P., Scandura, P., Vittori, G., 2004. Coherent structures in an oscillatory separated flow: numerical experiments. *Journal of Fluid Mechanics* 518, 215–229.
- Blondeaux, P., Vittori, G., 1991. Oscillatory flow and sediment motion over a rippled bed, in: 22th Int. Conf. on Coastal Engineering, Delft, The Netherlands.
- Carstens, M.R., Neilson, F.M., Altinbilek, H.D., 1969. Bed forms generated in the laboratory under an oscillatory flow : Analytical and experimental study. Technical report. U.S. Army, Corps of Engineers, Coastal Engineering Research Center, Washington, DC.
- Chang, Y.S., Scotti, A., 2003. Entrainment and suspension of sediments into a turbulent flow over ripples. *Journal of Turbulence* 4, 1–19.
- Cheng, N., Zhao, K., 2017. Difference between static and dynamic angle of repose of uniform sediment grains. *International Journal of Sediment Research* 32, 149–154.

- Cummings, D.I., Dumas, S., Dalrymple, R.W., 2009. Fine-grained versus coarse-grained wave ripples generated experimentally under large-scale oscillatory flow. *Journal of Sedimentary Research* 79, 83.
- Davies, A.G., Thorne, P.D., 2005. Modeling and measurement of sediment transport by waves in the vortex ripple regime. *Journal of Geophysical Research: Oceans* 110. doi:10.1029/2004JC002468.
- Davies, M.B.A., Villaret, C., 1994. Suspension of sand in oscillatory flow above ripples: discrete-vortex model and laboratory experiments, in: *Sediment transport mechanisms in coastal environments and rivers Proceedings of the EUROMECH 310 Conference*, World Scientific.
- Dingler, J., 1974. Wave-formed ripples in nearshore sands. Ph.D. thesis. University of California, San Diego, CA.
- Doucette, J.S., O'donoghue, T., 2006. Response of sand ripples to change in oscillatory flow. *Sedimentology* 53, 581–596.
- Du Toit, C.K., Sleath, J., 1981. Velocity measurements close to rippled beds in oscillatory flow. *Journal of Fluid Mechanics* 112, 71–96.
- Faraci, C., Foti, E., 2002. Geometry, migration and evolution of small-scale bedforms generated by regular and irregular waves. *Coastal Engineering* 47, 35–52.
- Fredsøe, J., Deigaard, R., 1992. *Mechanics of coastal sediment transport*, Advanced Series on Ocean Engineering. volume 3. World scientific, Singapore.

- Fujita, H., Yokosawa, H., Hirota, M., 1989. Secondary flow of the second kind in rectangular ducts with one rough wall. *Experimental Thermal and Fluid Science* 2, 72 – 80.
- Grant, W.D., Madsen, O.S., 1979. Combined wave and current interaction with a rough bottom. *Journal of Geophysical Research: Oceans* 84, 1797–1808.
- Grant, W.D., Madsen, O.S., 1982. Movable bed roughness in unsteady oscillatory flow. *Journal of Geophysical Research: Oceans* 87, 469–481.
- Humbyrd, C.J., 2012. Turbulent combined wave-current boundary layer model for application in coastal waters. Master's thesis. Massachusetts Institute of Technology. Cambridge, MA.
- Inman, D.L., 1957. Wave-generated ripples in nearshore sands. Technical Report. Scripps Institution of Oceanography La Jolla CA.
- Lofquist, K.E., 1978. Sand ripple growth in an oscillatory-flow water tunnel. Technical report. U.S. Army, Corps of Engineers, Coastal Engineering Research Center, Fort Belvoir, VA.
- Madsen, O.S., Wood, W., 2002. Sediment transport outside the surf zone. *Coastal Engineering Manual, Part III, Coastal Processes, Chapter 6*, U.S. Army Corps of Engineers, Washington, DC.
- Miller, M.C., Komar, P.D., 1980. A field investigation of the relationship between oscillation ripple spacing and the near-bottom water orbital motions. *Journal of Sedimentary Research* 50, 183–191.

- Nielsen, P., 1981. Dynamics and geometry of wave-generated ripples. *Journal of Geophysical Research: Oceans* 86, 6467–6472.
- Nielsen, P., 1984. Field measurements of time-averaged suspended sediment concentrations under waves. *Coastal Engineering* 8, 51–72.
- Nielsen, P., 1988. Three simple models of wave sediment transport. *Coastal Engineering* 12, 43–62. doi:[https://doi.org/10.1016/0378-3839\(88\)90014-2](https://doi.org/10.1016/0378-3839(88)90014-2).
- O’Donoghue, T., Clubb, G.S., 2001. Sand ripples generated by regular oscillatory flow. *Coastal Engineering* 44, 101–115.
- O’Donoghue, T., Doucette, J.S., van der Werf, J.J., Ribberink, J.S., 2006. The dimensions of sand ripples in full-scale oscillatory flows. *Coastal Engineering* 53, 997–1012.
- O’Donoghue, T., Wright, S., 2004. Flow tunnel measurements of velocities and sand flux in oscillatory sheet flow for well-sorted and graded sands. *Coastal Engineering* 51, 1163–1184.
- Pedocchi, F., García, M.H., 2009a. Ripple morphology under oscillatory flow: 1. prediction. *Journal of Geophysical Research: Oceans* 114, C12014.
- Pedocchi, F., García, M.H., 2009b. Ripple morphology under oscillatory flow: 2. experiments. *Journal of Geophysical Research: Oceans* 114, C12015.
- Ribberink, J.S., 1998. Bed-load transport for steady flows and unsteady oscillatory flows. *Coastal Engineering* 34, 59–82. doi:[10.1016/S0378-3839\(98\)00013-1](https://doi.org/10.1016/S0378-3839(98)00013-1).

- Ribberink, J.S., Al-Salem, A.A., 1994. Sediment transport in oscillatory boundary layers in cases of rippled beds and sheet flow. *Journal of Geophysical Research: Oceans* 99, 12707–12727.
- Shimamoto, T., Nielsen, P., Baldock, T., 2013. Updated “grab and dump” model for sediment transport under acceleration skewed waves, in: *Proc. Seventh Int. Conf. on Coastal Dynamics*, pp. 1495–1504.
- Traykovski, P., Hay, A.E., Irish, J.D., Lynch, J.F., 1999. Geometry, migration, and evolution of wave orbital ripples at leo15. *Journal of Geophysical Research: Oceans* 104, 1505–1524.
- Wang, D., Yuan, J., 2018. Bottom-slope-induced net sediment transport rate under oscillatory flows in the rippled-bed regime. *Journal of Geophysical Research: Oceans* doi:10.1029/2018JC013810.
- van der Werf, J.J., Doucette, J.S., O’Donoghue, T., Ribberink, J.S., 2007. Detailed measurements of velocities and suspended sand concentrations over fullscale ripples in regular oscillatory flow. *Journal of Geophysical Research: Earth Surface* 112, F02012.
- Wiberg, P.L., Harris, C.K., 1994. Ripple geometry in wave-dominated environments. *Journal of Geophysical Research: Oceans* 99, 775–789.
- Wikramanayake, P.N., Madsen, O.S., 1994. Calculation of movable bed friction factors. Technical Report. U.S. Army Engineer Waterways Experiment Station, Vicksburg, MS.
- Xu, J., 2005. Observations of plan-view sand ripple behavior and spectral

- wave climate on the inner shelf of san pedro bay, california. *Continental Shelf Research* 25, 373–396.
- Yuan, J., Dongxu, W., Madsen, O.S., 2017a. A laser-based bottom profiler system for measuring net sediment transport rate in an oscillatory water tunnel, in: *Proceedings of Coastal Dynamics 2017*.
- Yuan, J., Li, Z., Madsen, O.S., 2017b. Bottom-slope-induced net sheet-flow sediment transport rate under sinusoidal oscillatory flows. *Journal of Geophysical Research: Oceans* 122, 236–263.
- Yuan, J., Madsen, O.S., 2014. Experimental study of turbulent oscillatory boundary layers in an oscillating water tunnel. *Coastal Engineering* 89, 63–84.
- Yuan, J., Wang, D., 2018. Experimental investigation of total bottom shear stress for oscillatory flows over sand ripples. *Journal of Geophysical Research: Oceans* 123, 6481–6502.

Figure captions

Figure 1: Experimental facility and instruments: (a) illustrative sketch (side view) of the WCS; (b) LBP photo in a light background; (c) LBP photo in a dark background.

Figure 2: Time series of free-stream velocity (black dashed lines: sinusoidal flow; red solid line: skewed flow; blue solid line: asymmetric flow).

Figure 3: Development history of equilibrium 2-D ripples for Ta060: (a)-(c) measured data; (d)-(f) LBP photos.

Figure 4: Amplitude spectrum of bed profile: (a) absolute spectrum for Ta060; (b) normalized spectrum for Ta060; (c) absolute spectrum for Tb030; (d) normalized spectrum for Tb030.

Figure 5: Final bottom profile for Ta120 ($U_{bm} = 1184$ mm/s, $T = 6.25$ s, $\psi_{wmd} = 0.673$).

Figure 6: Development history of equilibrium 3-D ripples for Tb030: (a) global correlation coefficient; (b) ripple length (c) ripple height; (d)-(g) typical measured bottom profiles.

Figure 7: Illustrative sketch of secondary transverse flows and ripples with different scales.

Figure 8: Determination of representative ripple profile of test Ta040 (a) whole LBP-measured bottom profile; (b) collocated individual ripples; (c) representative ripple profile (grey zone: standard deviation).

Figure 9: Measured (subscript ‘m’) ripple dimensions against predicted equilibrium dimensions (subscript ‘p’) of Grant and Madsen (1982) for sinusoidal-flow-generated ripples (dots with circles: 3-D cases; black solid lines: perfect agreement; dashed lines: 20% deviation from perfect agreement; blue solid

lines: best fit through origin).

Figure 10: Comparison of normalized representative ripple profiles for sinusoidal flows (solid red lines) with DS81 profiles (dashed lines) and sinusoidal profiles (dashed dot lines).

Figure 11: Variation of similarity parameter β_ε with (a) Shields parameter ψ_{wmd} (dashed line: trend line connected by measurements of Ta-series tests) and (b) A_{bm}/λ .

Figure 12: Snapshots of sediment cloud in (a) a weak-flow test Ta040 and (b) a strong-flow test Ta080 (photos were taken when the strongest suspension occurred and the coherent vortex is highlighted by the dashed circle).

Figure 13: The roundness of ripple crest (a) definition of crest roundness based on a representative test Ta080; (b) variation of R_c with Shields parameter; (c) variation of normalized R_c/η with Shields parameter.

Figure 14: Variation of (a) maximum slope $\beta_{s,max}$ and (b) location $\gamma_{\beta,max}$ with Shields parameter ψ_{wmd} (dashed line: $\gamma_{\beta,max}=0.25$).

Figure 15: Typical example of vortex ripple under (a) skewed-flow condition Ta060S and (b) asymmetric-flow condition Ta060A (dashed lines: outline of ripple profiles).

Figure 16: Variation of ripple dimension due to flow nonlinearities: (a) ripple height and (b) ripple length; (subscript “sine” indicates data from sinusoidal-flow tests and “nonlinear” indicates data from “nonlinear”-flow tests).

Figure 17: Comparison of normalized representative ripple profiles (dashed lines: sinusoidal-flow-generated ripples; red solid lines: asymmetric-flow-

generated ripples; blue solid lines: skewed-flow-generated ripples; each row has the same first-harmonic oscillatory flow indicated by the test ID at the top-left corner).

Figure 18: Calculated shape factors for ripples generated in various flow conditions (black circles: sinusoidal flows; red squares: asymmetric flows; blue triangles: skewed flows).

Figure 19: Comparison of crest roundness of sinusoidal-flow-generated and “nonlinear”-flow-generated ripples.

Figure 20: Comparison of maximum slopes along ripple flanks for sinusoidal-flow-generated and “nonlinear”-flow-generated ripples: (a) offshore flank; (b) onshore flank.

Table 1: Summary of previous studies on ripple geometry

Reference	Facility ^a	Grain size [mm]	Flow type ^b	Re	Ripple shape ^c
Bagnold and Taylor (1946)	OST	0.09-2.50	Sine	$O(10^2 - 10^3)$	G
Lofquist (1978)	OWT	0.18,0.21,0.55	Sine	$8.5 \times 10^4 - 2.1 \times 10^5$	-
Du Toit and Sleath (1981)	OST&OWT	0.41	Sine	$6.3 \times 10^3 - 5.6 \times 10^4$	D
Ribberink and Al-Salem (1994)	OWT	0.21	Sine&V-skw	$9.8 \times 10^4 - 5.7 \times 10^6$	-
Faraci and Foti (2002)	WT	0.25	V-skw	$3.2 \times 10^3 - 6.9 \times 10^4$	G
Davies and Thorne (2005)	WF	0.33	V-skw	$1.1 \times 10^5 - 3.4 \times 10^5$	G
O'Donoghue et al. (2006)	OWT	0.22,0.35,0.44	V-skw	$7.9 \times 10^4 - 1.1 \times 10^6$	-
Doucette and O'donoghue (2006)	OWT	0.44	V-skw	$8.5 \times 10^4 - 3.1 \times 10^5$	D
Pedocchi and García (2009b)	OWT	0.25	Sine	$2.0 \times 10^4 - 9.6 \times 10^5$	G
Inman (1957)	Field	0.12-0.50	F	$O(10^4 - 10^5)$	G
Dingler (1974)	Field	0.12-0.61	F	$7.9 \times 10^4 - 1.1 \times 10^6$	G
Miller and Komar (1980)	Field	0.16-0.28	F	$1.6 \times 10^4 - 4.5 \times 10^5$	-
Nielsen (1984)	Field	0.11-0.62	F	$O(10^5)$	-
Traykovski et al. (1999)	Filed	0.33-0.46	F	$O(10^5)$	G
Xu (2005)	Field	0.09	F	$O(10^4 - 10^5)$	-

^a OST: Oscillating sand tray; OWT: Oscillatory water tunnel; WT: Wave tank; WF: Wave flume.

^b Sine: Sinusoidal flows; V-skw: Velocity-skewed flows; F: Field waves;

^c -: very little information was provided; G: general and qualitative comments were provided; D: Detailed measurements were provided.

Table 2: Summary of experiments for sinusoidal flows over coarse sand ($d_{50} = 0.51\text{mm}$)

Flow condition ^a	Initial bed ^b	T [s]	U_{bm} [mm/s]	A_{bm} [mm]	ψ_{wmd}	Re_w	Planform	# of ripples	T_d [h]	$\lambda[\text{mm}] \pm \sigma_\lambda^*$	$\eta[\text{mm}] \pm \sigma_\eta^*$	η/λ	A_{bm}/λ
Ta030(1)	F	6.25	296	294	0.062	8.66×10^4	2-D	18	4.0	$398 \pm 4\%$	$79 \pm 8\%$	0.20	0.74
Ta040(2)	F	6.25	395	393	0.102	1.54×10^5	2-D	17	3.2	$455 \pm 5\%$	$92 \pm 7\%$	0.20	0.86
Ta045(1)	F	6.25	444	442	0.122	1.94×10^5	2-D	16	2.1	$501 \pm 3\%$	$94 \pm 3\%$	0.20	0.88
Ta050(1)	F	6.25	493	490	0.149	2.41×10^5	2-D	16	1.4	$529 \pm 1\%$	$101 \pm 7\%$	0.19	0.95
Ta060(3)	F	6.25	592	589	0.203	3.46×10^5	2-D	13	1.0	$569 \pm 2\%$	$106 \pm 5\%$	0.19	1.04
Ta080(4)	F	6.25	790	786	0.333	6.16×10^5	2-D	10	0.5	$710 \pm 4\%$	$129 \pm 4\%$	0.18	1.11
Ta100(1)	F	6.25	987	982	0.490	9.62×10^5	2-D	9	0.3	$805 \pm 1\%$	$114 \pm 4\%$	0.14	1.22
Ta120(1)	F	6.25	1184	1178	0.673	1.39×10^6	Sheet-flow	N.A.	0.2	N.A.	N.A.	N.A.	N.A.
Tb030(1)	F	4.17	296	196	0.073	5.77×10^4	3-D	26	17.2	$242 \pm 6\%$	$41 \pm 11\%$	0.17	1.22
Tb060(2)	F	4.17	592	393	0.228	2.31×10^5	2-D	17	2.3	$447 \pm 1\%$	$75 \pm 8\%$	0.17	0.88
Tb075(5)	F	4.17	740	491	0.334	3.60×10^5	2-D	16	1.9	$522 \pm 2\%$	$80 \pm 3\%$	0.15	0.94
Tc040(2)	F	3.13	394	196	0.129	7.68×10^4	3-D	32	6.9	$202 \pm 6\%$	$28 \pm 14\%$	0.14	0.97
Td045(1)	F	8.33	444	589	0.114	2.60×10^5	2-D	13	1.1	$606 \pm 4\%$	$123 \pm 3\%$	0.20	0.97
Td060(1)	R _{Td045}	8.33	592	785	0.188	4.62×10^5	2-D	11	0.8	$750 \pm 3\%$	$143 \pm 8\%$	0.19	1.05
Td075(1)	R _{Td060}	8.33	741	982	0.276	7.22×10^5	2-D	8	1.3	$904 \pm 1\%$	$174 \pm 6\%$	0.19	1.09
Te044(1)	F	10.00	432	688	0.103	2.95×10^5	2-D	9	3.3	$883 \pm 2\%$	$177 \pm 5\%$	0.20	0.78

^aThe number in the brackets indicate the number of repeats for the typical flow condition.

^b “F” means flat bed and “R” means equilibrium rippled-bed at a certain flow condition (indicated by the subscript).

Table 3: Summary of experiments for “nonlinear”-flows over coarse sand ($d_{50} = 0.51\text{mm}$)

Test index ^a	T [s]	U_{bm} [mm/s]	λ [mm] $\pm\sigma_{\lambda}^*$	η [mm] $\pm\sigma_{\eta}^*$	Asy	Skw
<i>Ta040A</i>	6.25	395	489 \pm 6%	87 \pm 3%	0.0712	0.1465
<i>Ta040S</i>	6.25	395	413 \pm 4%	79 \pm 5%	0.1349	0.0066
<i>Ta045A</i>	6.25	444	569 \pm 2%	91 \pm 4%	0.0042	0.1928
<i>Ta045S</i>	6.25	444	464 \pm 3%	88 \pm 4%	0.1108	-0.0037
<i>Ta060A</i>	6.25	592	651 \pm 1%	108 \pm 4%	-0.0363	0.1030
<i>Ta060S</i>	6.25	592	513 \pm 4%	96 \pm 4%	0.1129	-0.0063
<i>Ta080A</i>	6.25	790	784 \pm 3%	115 \pm 8%	-0.0334	0.1184
<i>Ta080S</i>	6.25	790	644 \pm 2%	113 \pm 5%	0.0849	-0.0066
<i>Tb060A</i>	4.17	592	452 \pm 3%	64 \pm 3%	-0.0059	0.0989
<i>Tb060S</i>	4.17	592	393 \pm 3%	80 \pm 5%	0.0868	0.0393
<i>Tb060A</i>	8.33	592	877 \pm 5%	151 \pm 9%	-0.0043	0.0407
<i>Tb060S</i>	8.33	592	735 \pm 3%	133 \pm 3%	0.0482	-0.0038

^a Test index ending with “A” indicates asymmetric flows while “S” indicates skewed flows.

Figure 1:

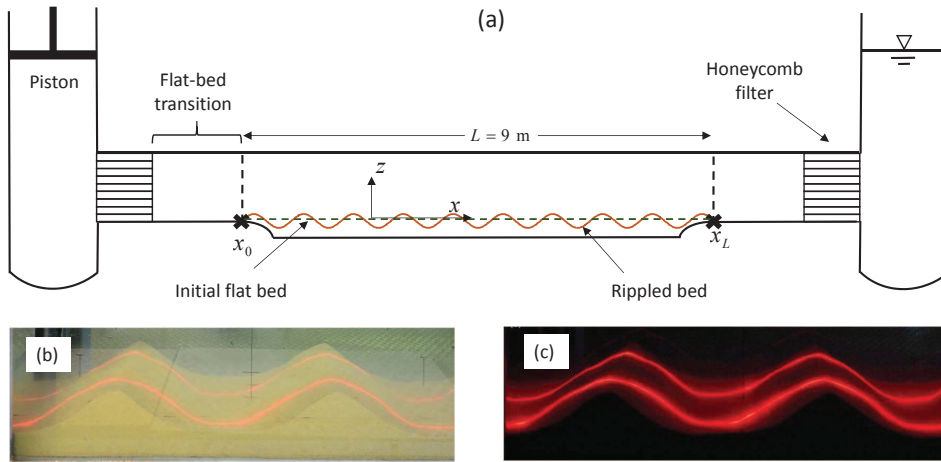


Figure 2:

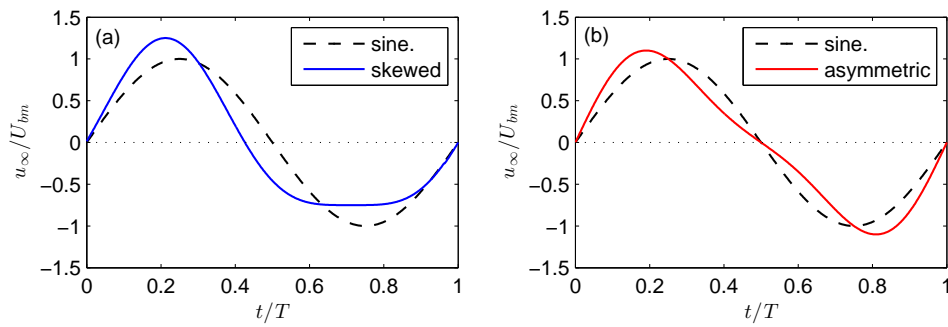


Figure 3:

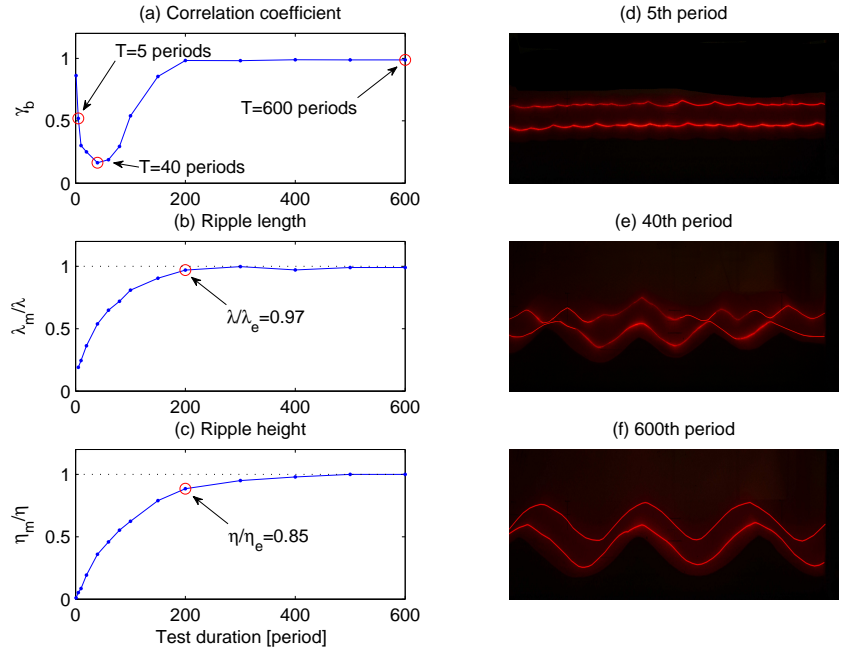


Figure 4:

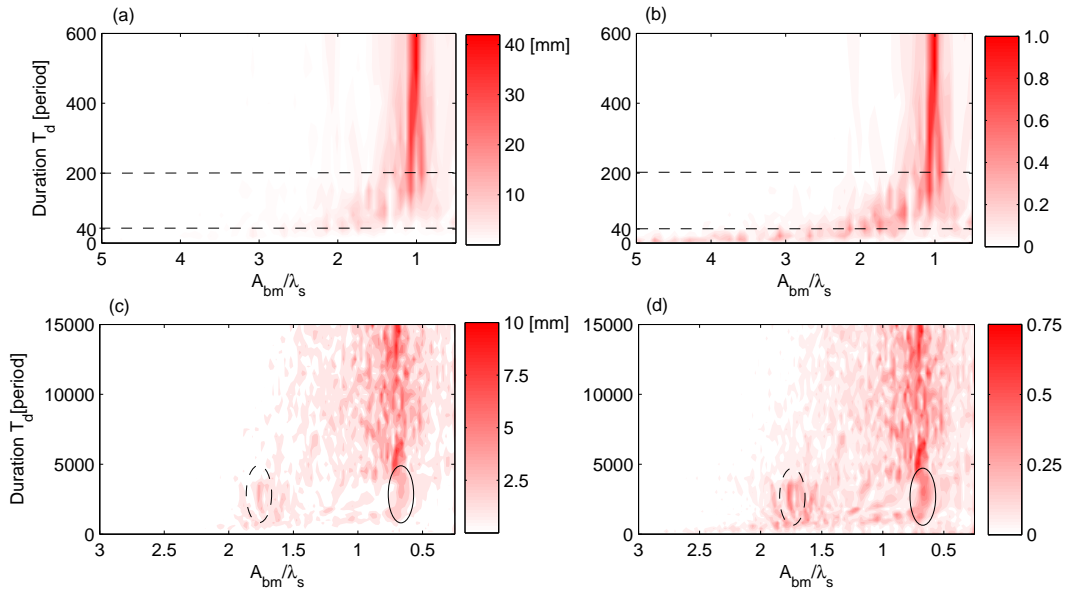


Figure 5:

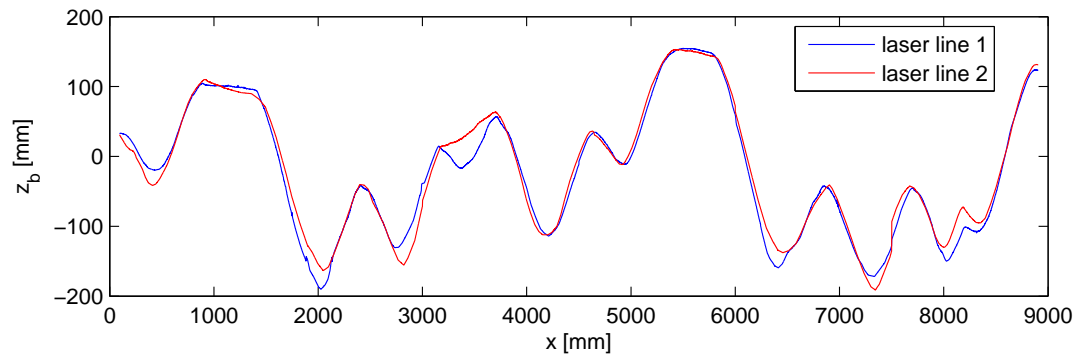


Figure 6:

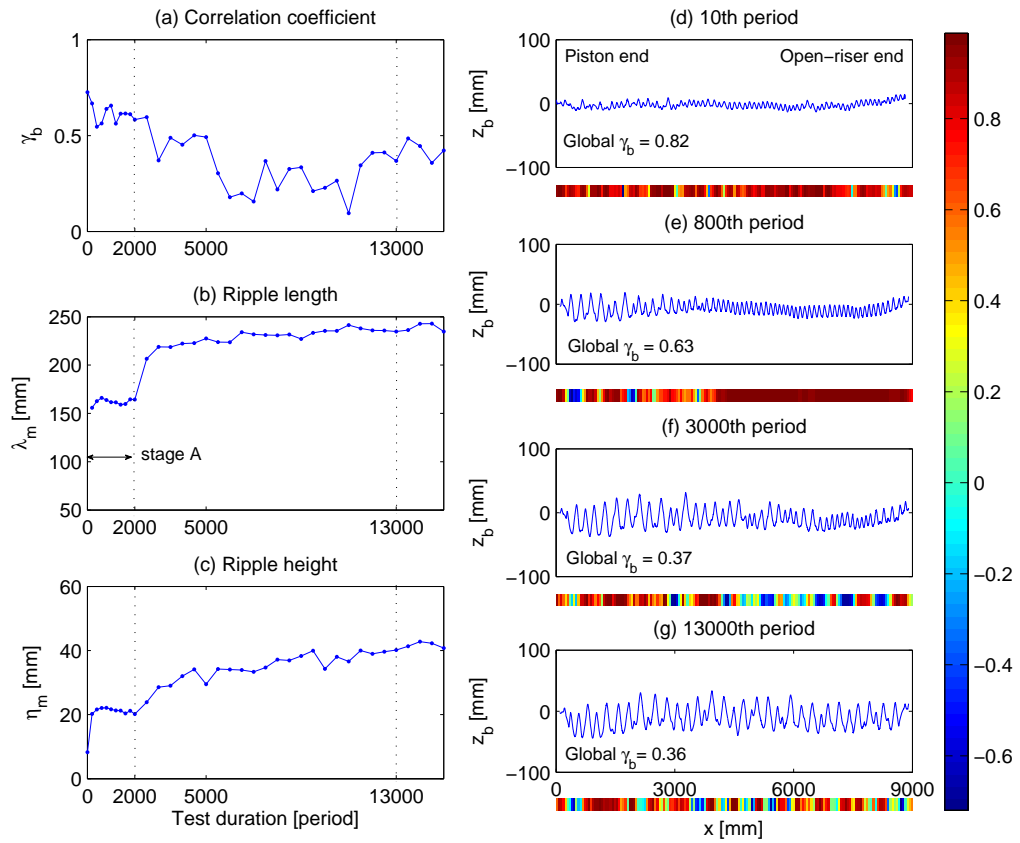


Figure 7:

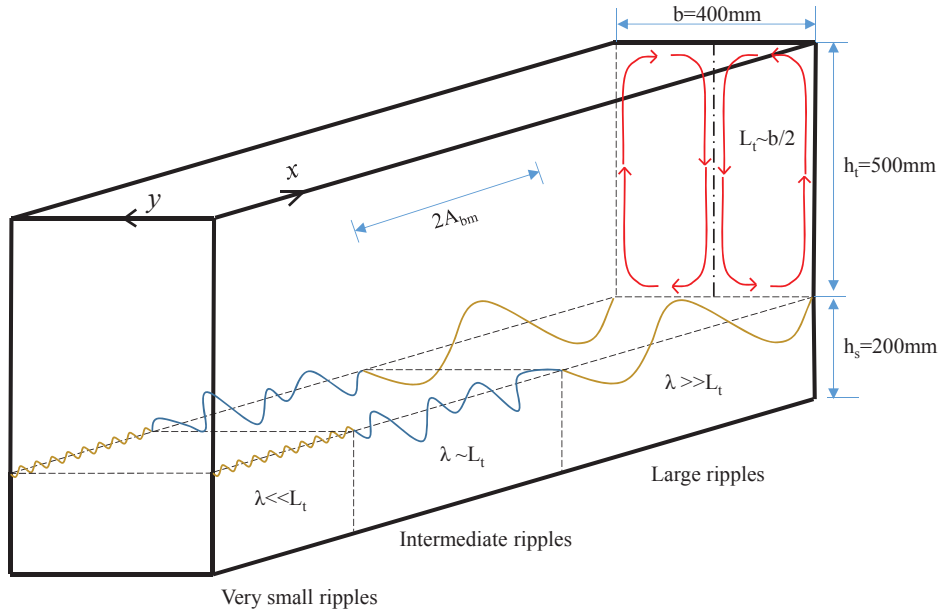


Figure 8:

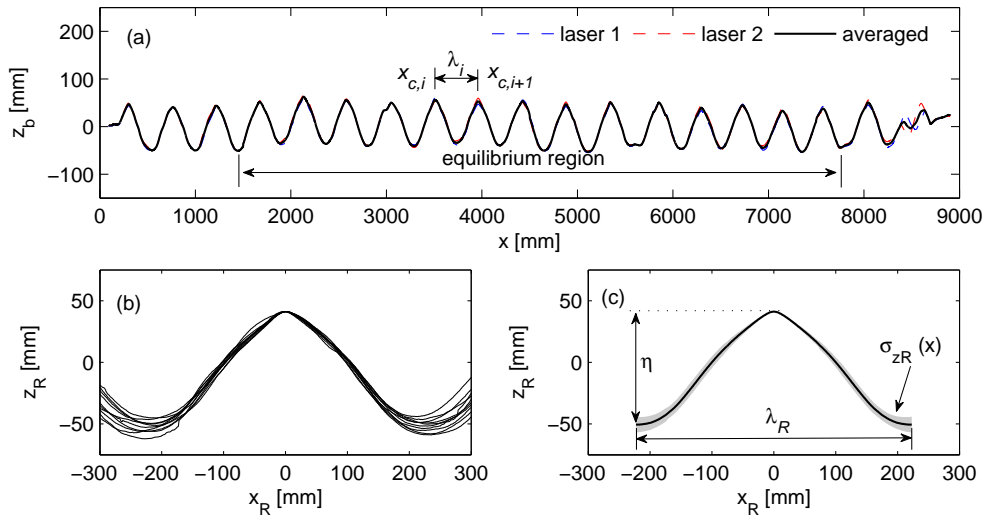


Figure 9:

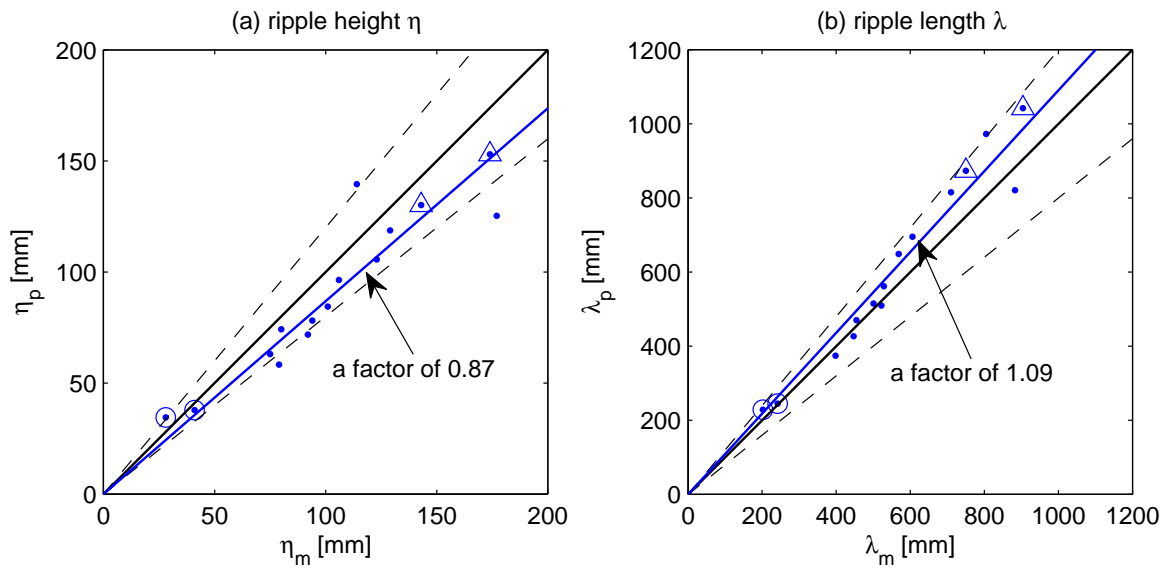


Figure 10:

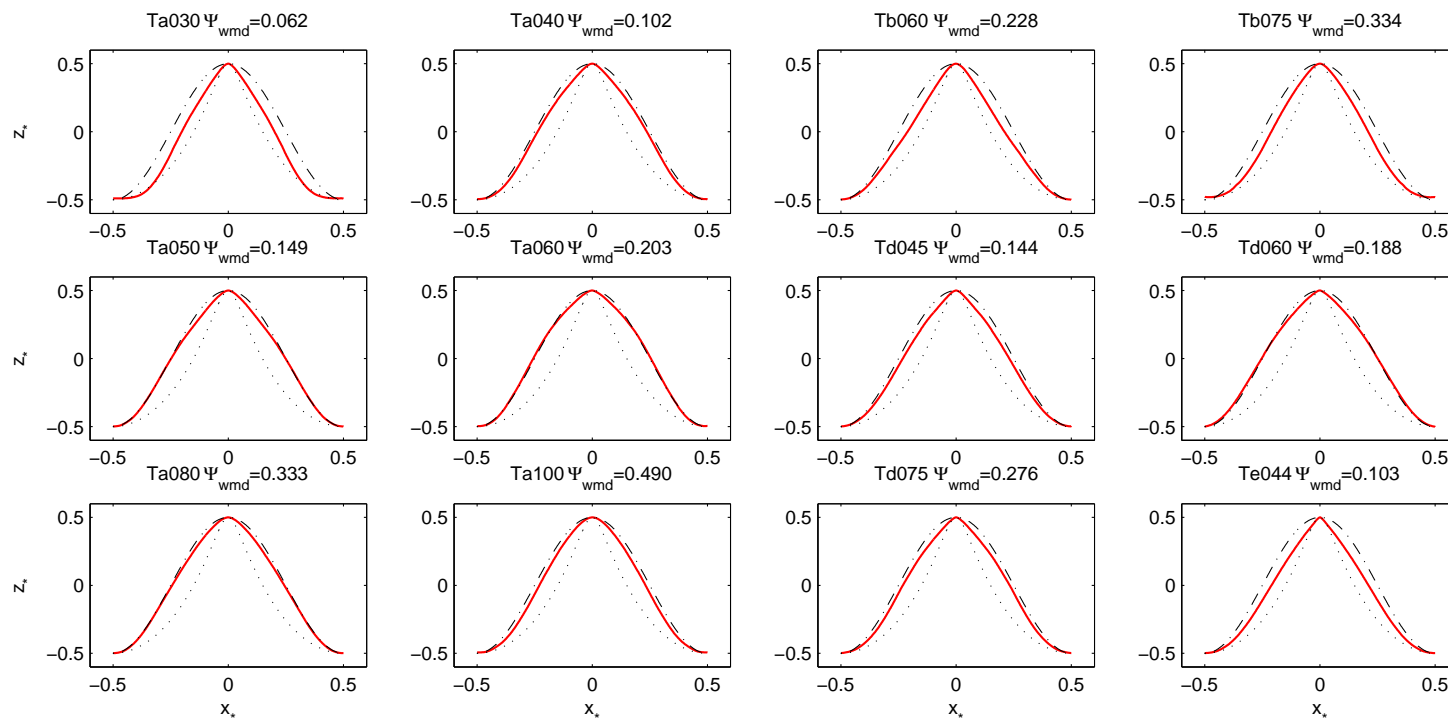


Figure 11:

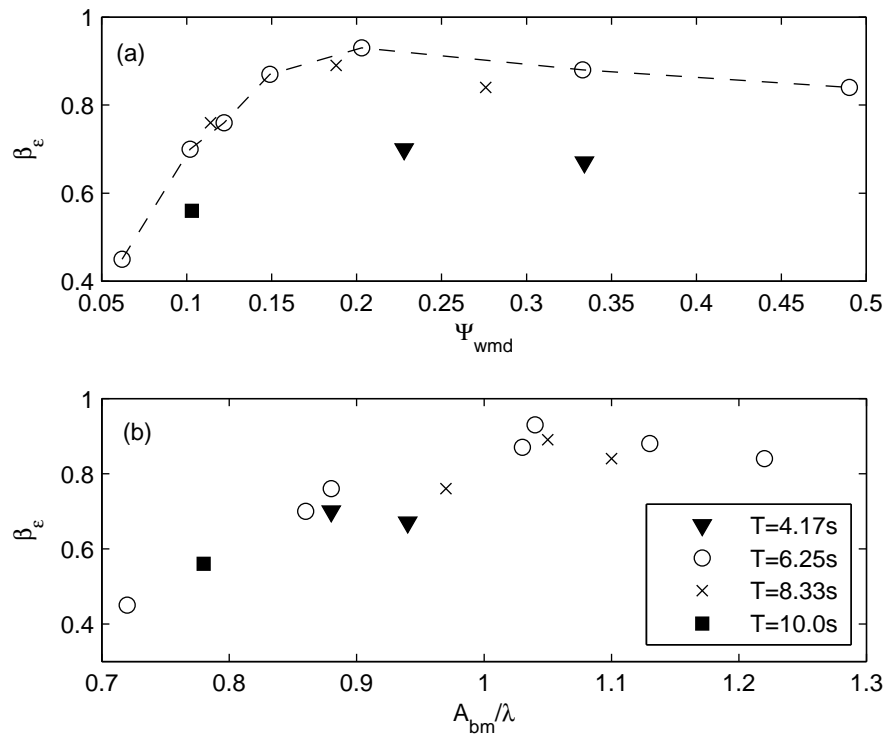


Figure 12:

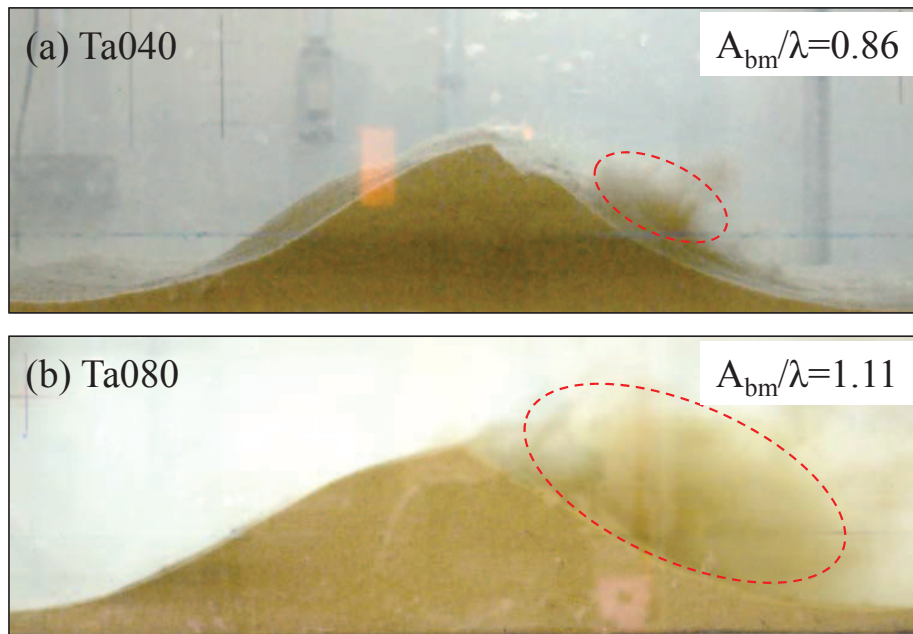


Figure 13:

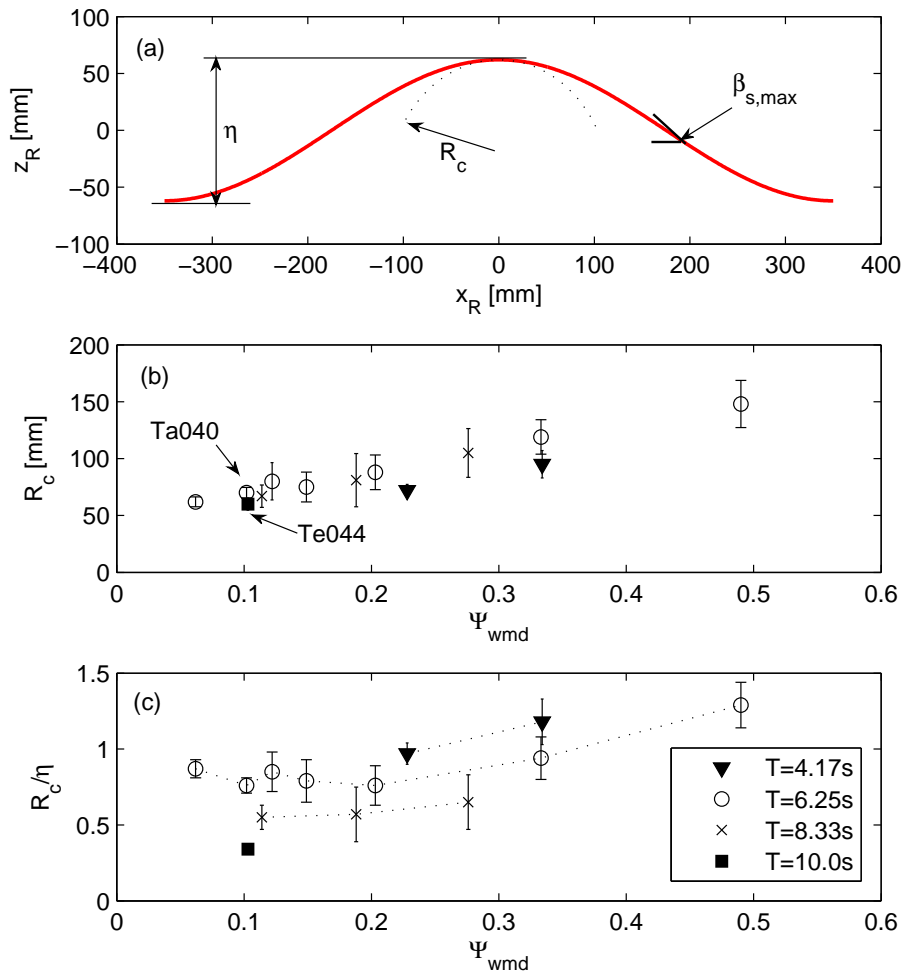


Figure 14:

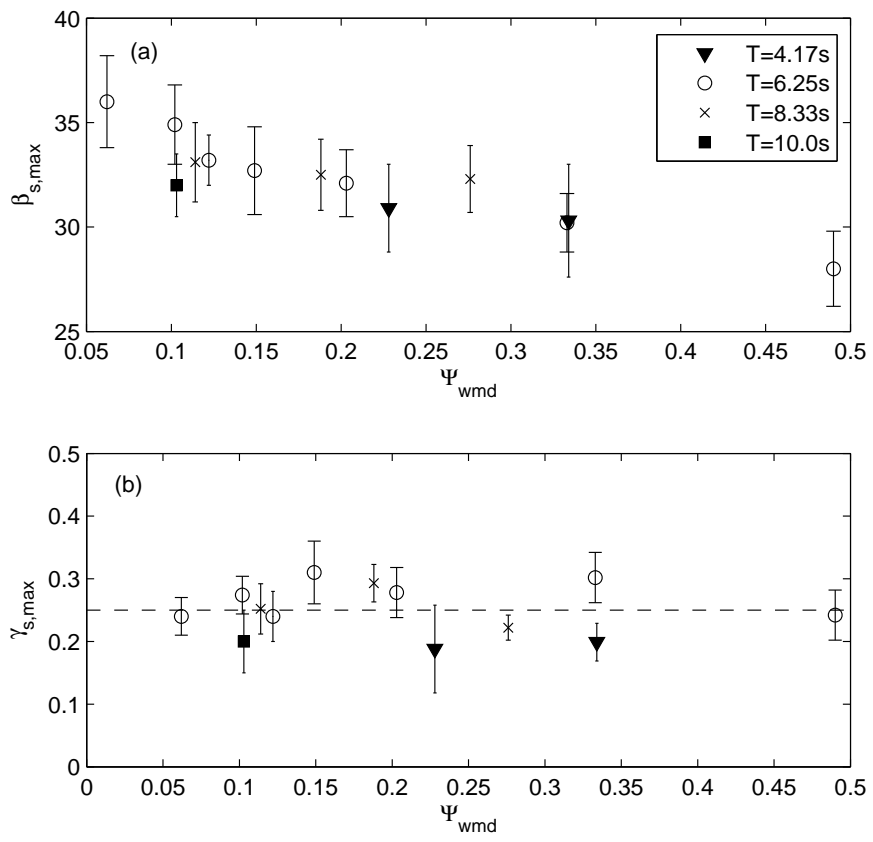


Figure 15:

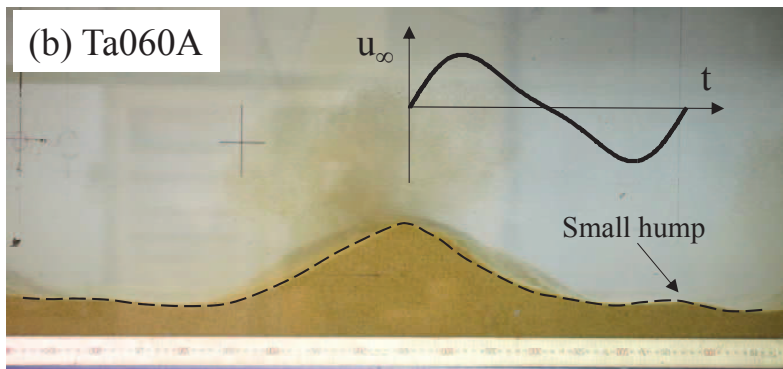
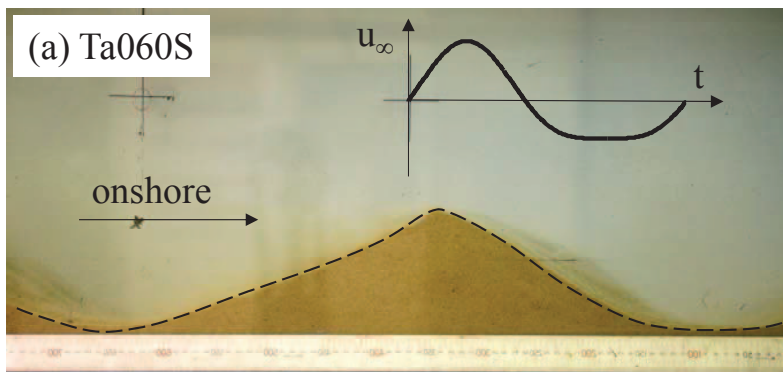


Figure 16:

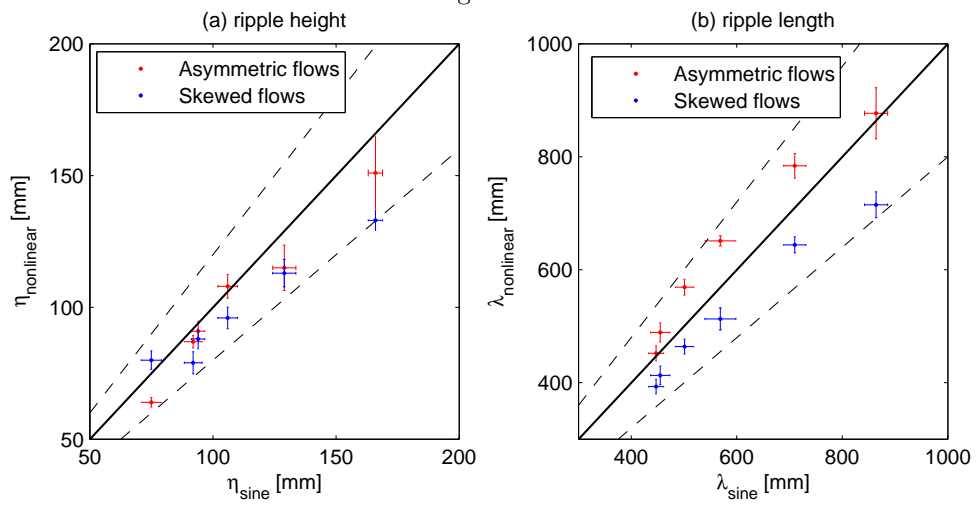


Figure 17:
onshore direction \rightarrow

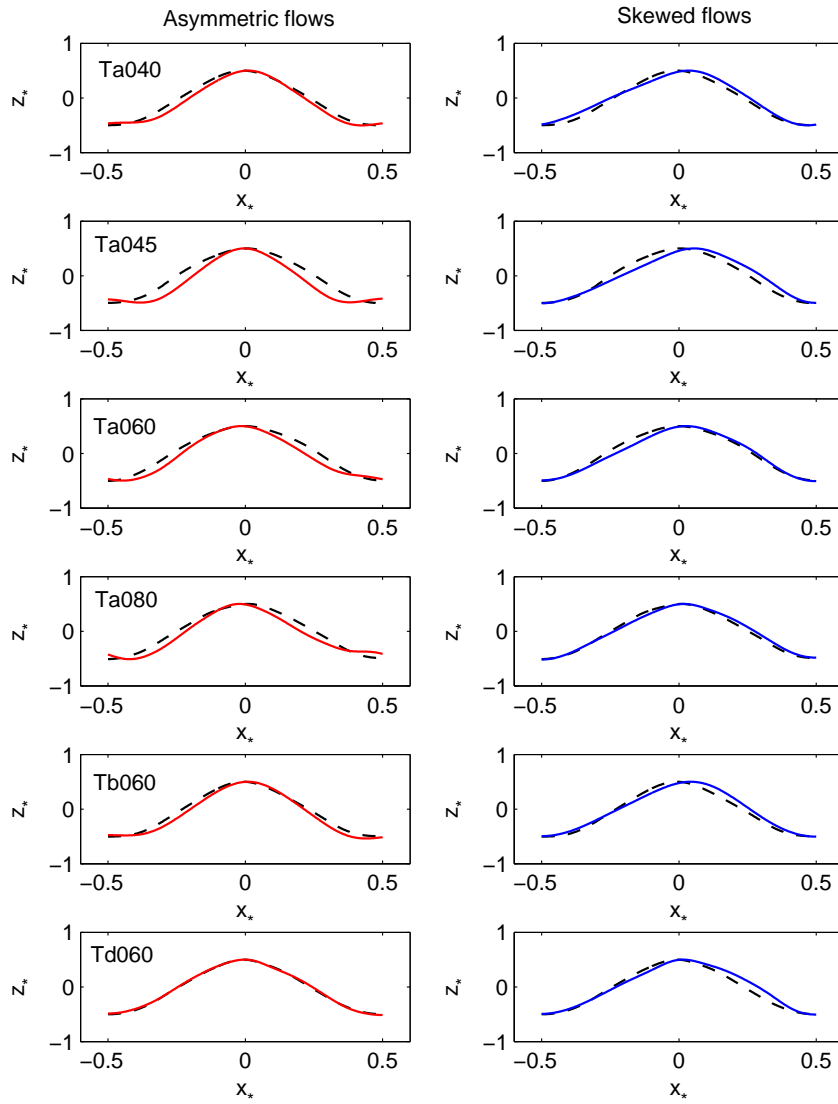


Figure 18:

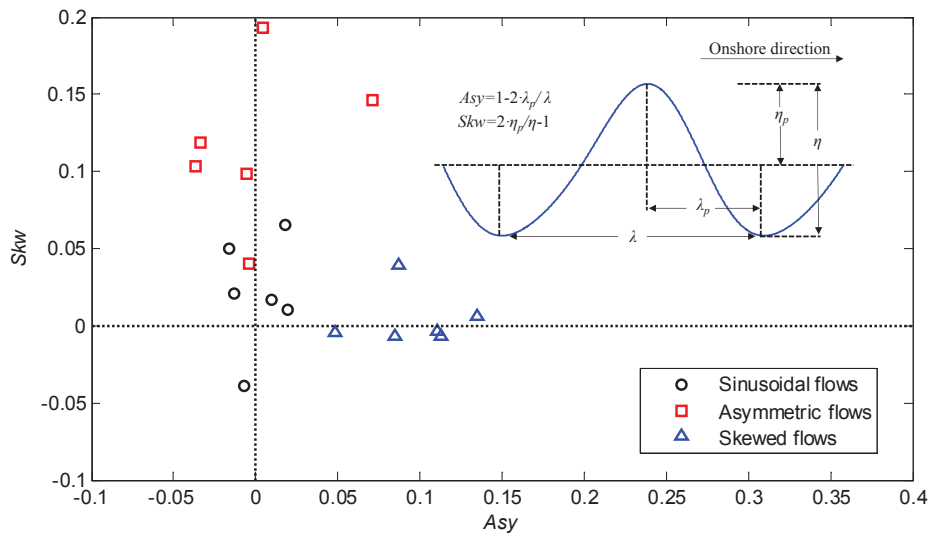


Figure 19:

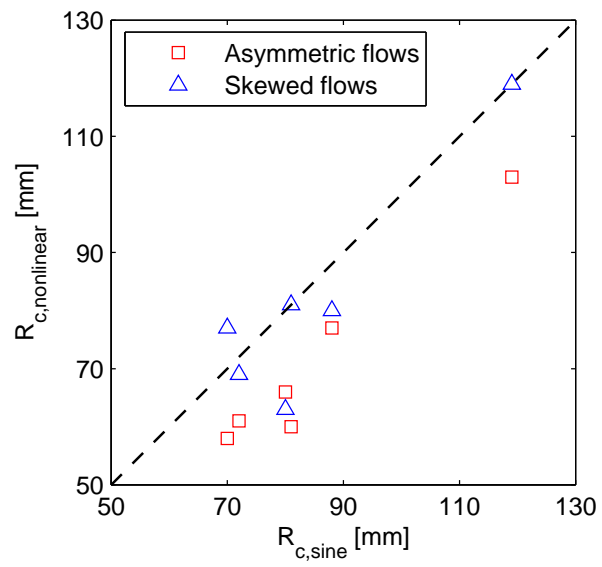


Figure 20:

